LOW-COST CERAMIC COMPOSITE MEMBRANES FOR FILTRATION OF PRODUCED WATER

By

CHRISTINE ANN WATSON

Bachelor of Science in Chemical Engineering
North Carolina State University
Raleigh, NC
2009

Bachelor of Science in Physics
North Carolina State University
Raleigh, NC
2009

Submitted to the Faculty of the
Graduate College of the
Oklahoma State University
in partial fulfillment of
the requirements for
the Degree of
MASTER OF SCIENCE
December, 2021

LOW-COST CERAMIC COMPOSITE MEMBRANES FOR FILTRATION OF PRODUCED WATER

Thesis Approved:

Dr. Pankaj Sarin

Thesis Adviser

Dr. Raman P. Singh

Dr. Krishnan Ranji Vaidyanathan

ACKNOWLEDGEMENTS

I would like to acknowledge the Oklahoma State University Office of the Vice President of Research for funding this work.

I am sincerely grateful for my advisor, Dr. Pankaj Sarin, my greatest source of encouragement along this graduate journey. I will be forever thankful for the opportunity to grow as a student and researcher under his wisdom, guidance, and mentorship. Thank you for lifting me up through many failures, pushing me onward through many challenges, believing in me when I climbed uphill battles, and celebrating with me on my achievements.

I would like to extend my deepest appreciation to my committee members, Dr. Raman P. Singh, and Dr. Krishnan Ranji Vaidyanathan. You have taught me to not let obstacles stop me from pursuing and pushing and going for my dreams. Thank you to my colleagues and fellow research group members for selflessly teaching and helping me along the way. I am proud to call you not just colleagues, but friends.

Finally, I dedicate this thesis in honor of my late father, who was incredibly proud that I would be a Cowboy. Although he did not get to see the completion of this thesis, he understood it, believed in it, and was excited about the impact it would have on the world.

Name: CHRISTINE ANN WATSON

Date of Degree: DECEMBER, 2021

Title of Study: LOW-COST CERAMIC COMPOSITE MEMBRANES FOR FILTRATION OF PRODUCED WATER

Major Field: MATERIALS SCIENCE AND ENGINEERING

Abstract: A by-product of the extraction of oil and gas from underground rock formations, naturally occurring water known as "produced water" is brought up to the surface. High in oil and salt concentrations that are expensive to remove, it is more financially feasible to dispose of produced water in underground injection wells than to treat and reuse, despite the long-term environmental effects. Meanwhile, more and more countries are being concerned about the decreasing global drinking water supply amid growing world population and rising temperatures due to global warming.

A low-cost treatment method of produced water would not only provide financial incentive for treatment over disposal, eliminating the subsequent environmental side effects of disposal in underground injection wells, but also enhance the global water supply by generating non-potable water for agricultural and industrial use.

With their robust thermal and chemical stability as well as long lifespans and environmentally-friendly materials, ceramic membranes are ideal for wastewater applications but traditionally have come at too high a cost to be used with produced water. In this study, a low-cost self-supporting ceramic composite membrane was developed using potassium-based geopolymer, clinoptilolite zeolite filler, and perforated aluminum support. The composition and processing methods for the membrane were optimized, and membrane microstructure was analyzed.

Filtration performance of the geopolymer composite membranes was tested using two different filtration modes: end-flow and cross-flow filtration. While end-flow is typically used for lab-scale filtration testing, cross-flow filtration is more practical for industrial applications. Principles of each type of filtration mode are explained, and flux of produced water through the membrane was measured. Filtration results were analyzed for removal of particulate impurities and dissolved solids. Strategies for improving membrane design and performance, as well as next steps toward industrial application, are outlined and discussed.

TABLE OF CONTENTS

Chapter Page

LIST OF TABLES

Table Page

Table Page

LIST OF FIGURES

Figure Page

Figure Page

Figure Page

Figure Page

CHAPTER I

REVIEW OF LITERATURE

As the world population grows at a dramatic rate, water consumption has increased for drinking water, agriculture, and industrial use. Combined with slowly rising temperatures due to global warming reducing rainfall and freshwater lake levels, the sustainability of the global water supply is becoming a topic of concern to scientists and technologists. At the same time, the underground injection of produced water is becoming more controversial due to the long-term environmental impacts, and recent legal regulations have sought to reduce the volume of injected produced water to protect surrounding communities.

1.1 Introduction to Produced Water

During the extraction of oil and gas from underground rock formations, naturally occurring water high in hydrocarbon and salt concentrations is brought to the surface. Known as "produced water" and considered an industrial waste, the cost of disposal of produced water is a major factor in the startup and operation costs of new oil and gas developments.

An estimated 21 billion barrels of produced water are generated each year in the United States, 97% from onshore oil and gas activities and 3% from offshore activities [1]. Large quantities of onshore produced water are reused and reinjected for enhanced oil recovery, with the remaining produced water disposed through underground injection wells. Of onshore operations, reinjected produced water is reportedly 1.8 to 4 times as much as that disposed underground [2]. As part of the reinjection process, industrial chemicals are added to improve extraction, resulting in a diverse range of chemicals that may contribute to the chemical makeup of produced water.

On the other hand, offshore produced water is typically treated through a variety of chemical and physical separation processes before being discharged into the ocean. Offshore produced water is typically not used for reinjection, due to low volumes of produced water and a preference for seawater for enhanced oil recovery [2].

Despite increasing concern for the long-term environmental impact of underground injection wells, disposal remains much more cost-effective than the treatment and reuse of produced water.

Meanwhile, the United States and other countries are becoming more and more interested in solutions to address water scarcity and security [3]. A low-cost treatment method of produced water would not only provide financial incentive for treatment over disposal, minimizing the environmental side effects of disposal in underground injection wells, but also contribute to the global water supply by generating non-potable water for agricultural and industrial use.

The components of produced water can vary greatly; factors include regional geological rock formations, industrial chemicals used for extraction, and variation due to reinjection. As seen in the Table 1.1, produced water is dominated by concentrations of total dissolved solids (TDS) and salt ions (Na^+, Cl^-).

Table 1.1 Components of Produced Water [4]. Abbreviations used: chemical oxygen demand (COD), total suspended solids (TSS), total organic carbon (TOC), total dissolved solids (TDS), Benzene toluene ethylbenzene xylene (BTEX).

Parameter	**Concentration (mg/L)**	**Parameter**	**Concentration (mg/L)**
Major Parameters		**Metals**	
COD	1220 – 2600	Na	0 – 150,000
TSS	1.2 – 1000	Sr	0 – 6250
TOC	0 – 1500	Zn	0.01 – 35
TDS	100 – 400,000	Li	0.038 – 64
Total Organic Acids	0.001 – 10,000	Al	0.4 – 410
Production Treatment Chemicals		As	0.002 – 11
		Ba	0 – 850
Corrosion Inhibitor	0.3 – 10	Cr	0.002 – 1.1
Scale Inhibitor	0.2 – 30	Fe	0.1 – 1100
BTEX		Mn	0.004 – 175
Benzene	0.032 – 778.51	K	24 – 4300
Ethylbenzene	0.026 – 399.84	Pd	0.008 – 0.88
Toluene	0.058 – 5.86	Ti	0.01 – 0.7
Xylene	0.01 – 1.29	**Other Ions**	
Total BTEX	0.73 – 24.1	B	5 – 95
Other Pollutants		Ca^{2+}	0 – 74,000
Saturated Hydrocarbons	17 – 30	SO_4^{2-}	0 – 15,000
Total Oil and Grease	2 – 560	Mg^{2+}	0.9 – 6,000
Phenol	0.001 – 10,000	HCO_3^-	0 – 15,000
		Cl^-	0 – 270,000

Current treatment methods utilize multi-step separation processes. Common separation processes include use of hydrocyclones, thermal separation, sand filtration, electrodialysis, adsorption, chemical treatment methods, and membrane filtration [5]. Hydrocyclones are typically used for physical separation of solids, sand, and oil from produced water, but have problems with solid and scale buildup, are unable to remove any dissolved materials so require extensive post-treatment processes. Thermal separation processes come at too high energy costs for widespread use. Sand filtration, electrodialysis, and adsorption processes require multiple pre-treatment steps and are used as end-step treatment processes. Chemical treatment methods have been used for removal of suspended solids but are not ideal for large-scale use and introduce potential toxicity from the chemicals used. Finally, existing membrane filtration processes currently take the form of capillary, hollow fiber, or tubular membranes that come at high capital costs with low flux through the membranes. Interest has increased in recent years to develop improved membrane filtration for produced water that can come at lower costs and higher yield of treated water.

1.2 Membrane Filtration

Filtration systems remain an industry favorite for water treatment due to their ease of use, wide commercial availability, and mobility for on-site applications. Filtration processes are broadly characterized as microfiltration (MF), ultrafiltration (UF), nanofiltration (NF), or reverse osmosis (RO) based on the approximate pore size. These terms are used very generally, as the pore size range is not precisely defined. Microfiltration processes have approximate pores sizes ranging from 0.05 - 10 μm, ultrafiltration from 0.01 - 0.1 μm, nanofiltration from 0.001 - 0.01 μm, and reverse osmosis from 0.0001- 0.001 μm. Typical microfiltration membranes are used to remove suspended particles and bacteria, ultrafiltration for viruses, nanofiltration for divalent ions, and reverse osmosis for remaining monovalent ions and dissolves organics. As the membrane pore size decreases, cost and energy tend to increase, as well as the need for multi-step treatment processes. For example, to reduce fouling and ensure practical lifetimes of reverse osmosis membranes, wastewater must be pretreated with ultra- or nanofiltration membranes [6].

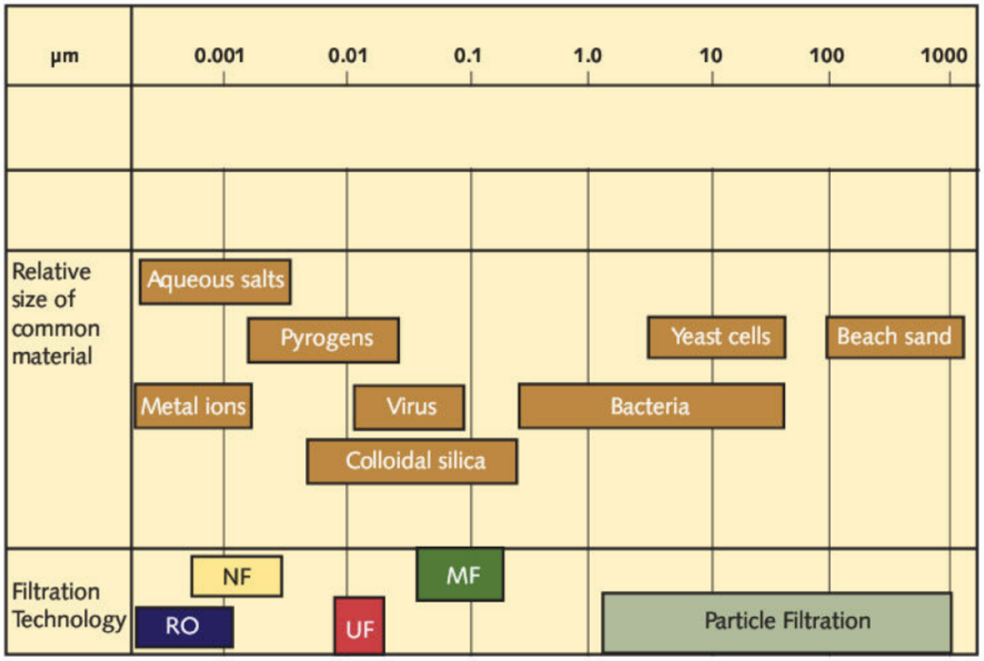

Figure 1.1 Common applications and pore size of filtration technologies [6].

1.2.1 Principles of End-flow Filtration

The most widely recognized setup for filtration is known as end-flow (or “dead-end” or “through-flow” filtration). In this setup, applied pressure moves a feed stream through a porous membrane. Particles that are too large to pass through the membrane accumulate on the surface in a cake layer, eventually reducing flux of wastewater through the membrane. A schematic of end-flow filtration is shown in Figure 1.2.

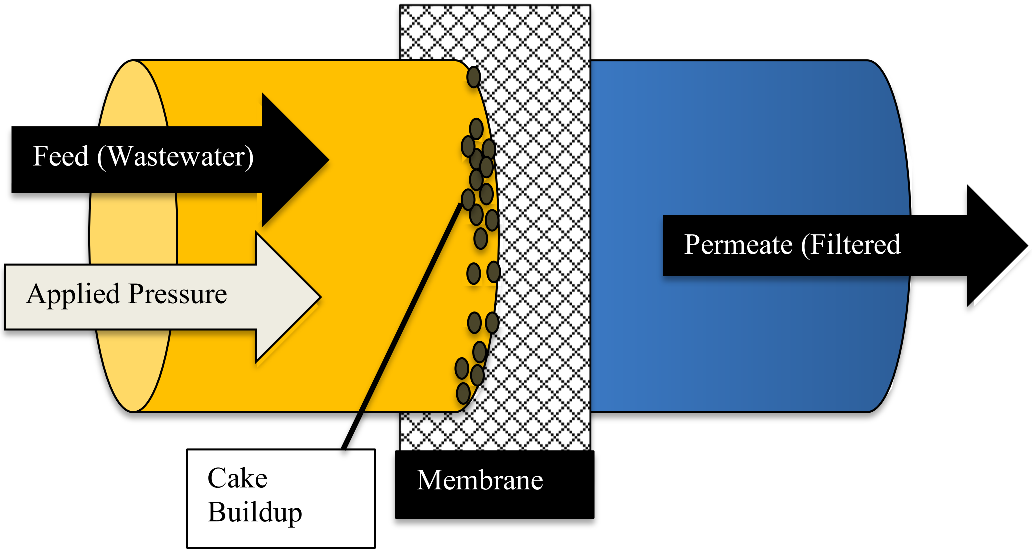

Figure 1.2 Schematic of end-flow filtration.

Assuming a Newtonian fluid, parabolic velocity profile, laminar flow, idealized straight cylindrical pores, and ignoring caking, the flux through a porous membrane can be approximated using the Hagen-Poiseuille law [7].

$$N = \frac{\epsilon \rho D^2}{32 \mu l_M}(P_0 - P_L)$$

Where N = bulk-flow flux (mass velocity) through the membrane, ϵ = porosity of the membrane (void fraction), ρ = fluid density, D = pore diameter, μ = fluid viscosity, l_M = membrane thickness, P_0 = pressure of filtered flow, and P_L = pressure of feed flow. Thus, optimal flux through a porous membrane can be controlled by varying the porosity of the membrane, pore size, membrane thickness, and pressure difference across the membrane.

Taking into account resistance due to caking, Darcy's Law provides a general description of the flux through a porous membrane in end-flow filtration:

$$J = \frac{\Delta P}{\mu(R_m - R_c)}$$

where J =liquid flux, μ = fluid viscosity, R_m = resistance due to the membrane material, and R_c = resistance due to the cake layer. R_m depends on pore-size distribution, porosity, and properties of the membrane material. As time progresses, the resistance due to the cake layer, R_c, becomes the dominating factor and reduces flux through the membrane [7]. Therefore, in addition to sufficient applied pressure, a membrane in end-flow filtration requires frequent cleaning due to caking of particles on the membrane surface.

1.2.2 Principles of Cross-flow Filtration

While end-flow filtration is appropriate for lab-scale testing, its inherent batch nature, as well as cost, frequent maintenance, and short membrane lifetimes make end-flow processes less desirable for industrial use. An alternative type of filtration process, cross-flow filtration (also known as “tangential flow”) is more ideal for continuous industrial-scale applications. A schematic of cross-flow filtration is shown in Figure 1.3. In cross-flow filtration, the feed stream flows parallel to the surface of the membrane. The term “retentate” refers to the wastewater stream after it has passed the membrane surface. The feed and retentate streams are operated under water pressure to ensure adequate flow past the membrane, and the permeate stream is usually held at atmospheric pressure. Therefore the pressure drop across the membrane acts as the driving force to pull filtered water through to the permeate stream. The retentate stream carries away the remaining particles and water. The cross-flow process can be done in multiple cascading stages with the retentate flowing to the feed stream of another membrane.

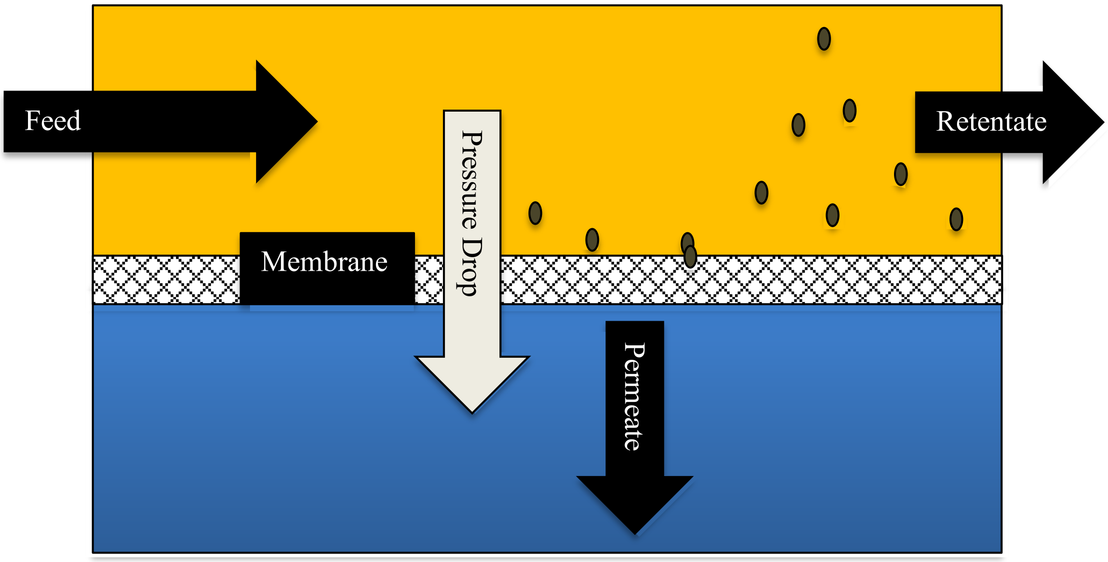

Figure 1.3 Schematic of cross-flow filtration.

Although cross-flow systems require the addition of retentate streams, increasing costs, they are much more efficient and environmentally friendly. Cross-flow filtration can be used to process large variations in particle size and solids concentrations, allow recycling streams for continuous flow, minimization of waste, and achievement of higher product yield than end-flow filtration [8]. A comparison of how well cross-flow and end-flow handle various wastewater conditions is shown in Table 1.2.

Table 1.2 Comparison of process conditions for cross-flow and end-flow filtration [8].

Process Conditions	**Cross-Flow Filtration**	**End-Flow Filtration**
Low solids (0-1% by volume)	Can handle efficiently but needs high flux to be cost effective	Can handle effectively; low cost
Medium solids (1-10% by volume)	Can adequately handle; economics depend on flux	Not well suited
High solids (10-70% by volume)	May not be economical at > 25% solids (with few exceptions) for continuous process	Not well suited
Emulsified liquids	Can handle efficiently	Not well suited
Small density difference or fine particles	Well suited due to wide range of pore diameters UF/MF	Can handle adequately
Separation of macromolecular solutes	Can handle very efficiently; cost effective alternative	Not well suited
Solvents and/or high temperature	Can handle adequately using chemically/thermally resistant membranes	Not well suited
Continuous fractionation of solids	Not well suited	Can handle but performance sensitive to operating conditions

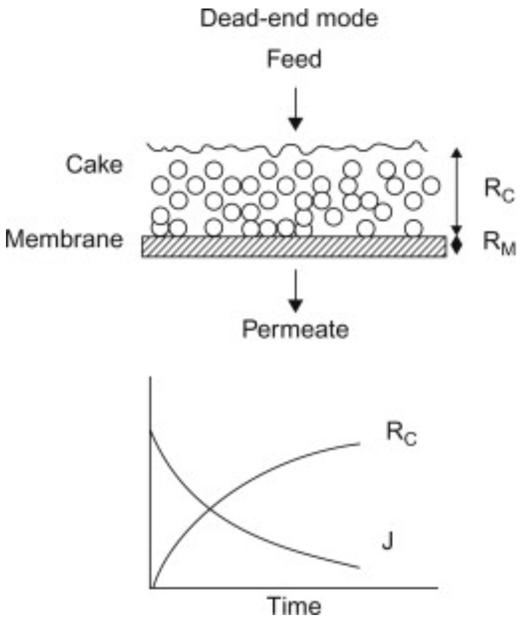

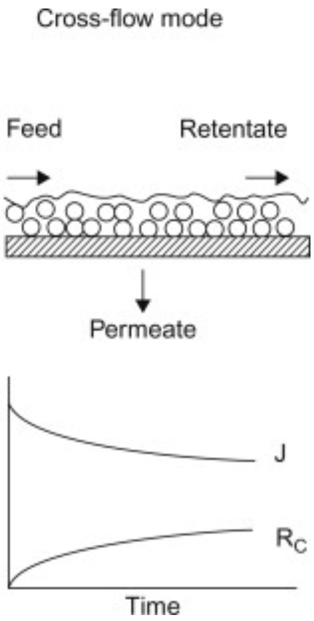

Figure 1.4 Comparison of permeate flux (J) and cake resistance (R_C) over time for dead-end and cross-flow modes [9].

Contrary to end-flow, the cake buildup layer in cross-flow filtration reaches a maximum steady thickness due to the shear flow of the retentate, allowing a steadier flux rate through the membrane (Figure 1.4), and reducing the need for frequent cleanings and increases the lifetime of the membrane.

The driving force in cross-flow filtration is related to the transmembrane pressure (TMP). The transmembrane pressure (TMP) can be calculated as $TMP = \left(\frac{P_{feed}+P_{retenate}}{2}\right) - P_{permeate}$, where $P_{permeate}$ is usually at atmospheric pressure [9].

Cross-flow filtration is often performed using tubular or spiral wound membranes, depending on the application. This allows maximum filtration efficiency and flux for a continuous system in an industrial application. An example of a spiral wound and tubular module for cross-flow are shown in Figure 1.5. In spiral wound membranes (Figure 1.5 A), the feed flows through the outer layers of a pipe while permeate flows through the center of the pipe in the opposite direction. In tubular membranes (Figure 1.5B), the feed flows into a collection of membrane tubes and permeate flows out the walls of the tubes.

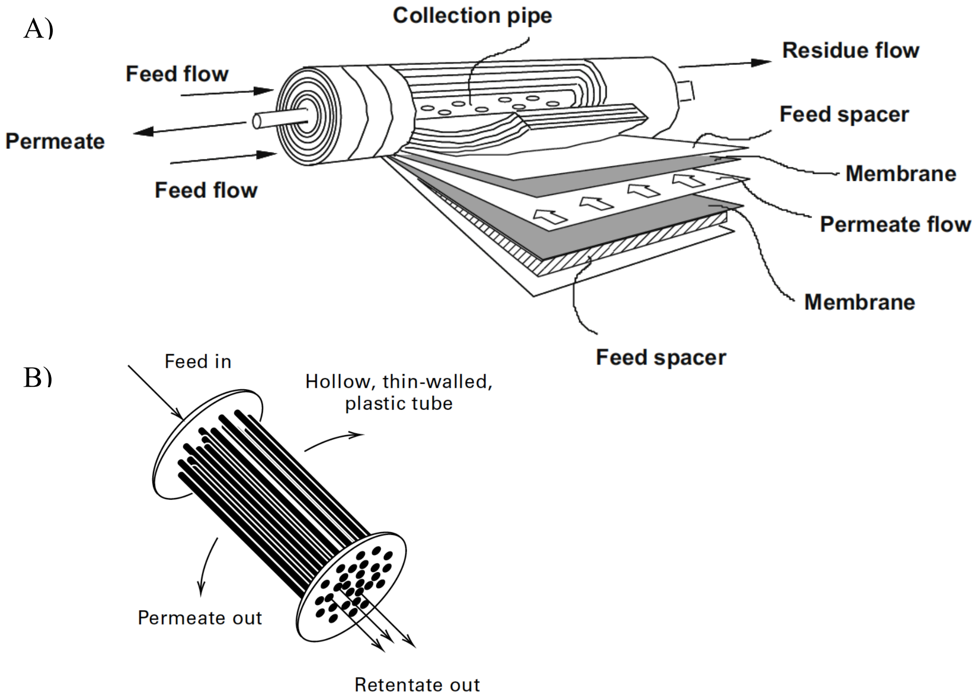

Figure 1.5 Common configurations of cross-flow membranes: A) Spiral wound module [11], B) Tubular module [7].

1.3 Ceramic Membranes

There are two main categories of commercial membranes are available: polymeric membranes and ceramic membranes. Polymeric membranes (such as acrylic, cellulose, nylon-based, polyamide, etc.) are generally cheaper, but are not appropriate for use in high temperatures (above 200 ºC) or under chemical exposure (such as strong acids.). Ceramic membranes (such as zirconia, titania, and alumina), on the other hand, have demonstrated strong thermal and chemical stability and longer lifespans, but at much higher costs. The high sintering temperatures and high cost of raw materials for ceramic membranes have limited them to small applications rather than widespread industry use [8-12].

1.3.1 Geopolymer Composite Membranes

By using low-cost raw materials to lower costs, environmentally friendly ceramic membranes have been the focus of recent attention for large scale water treatment projects in developing countries to address water scarcity [12]. One particular type of material, geopolymer ceramic, is a relatively new material of interest. First discovered by Davidovits in 1989 [13], geopolymers have attracted attention as an environmentally friendly alternative to Portland cement with their lower CO_2 emissions involved in processing and their use of inexpensive source materials for the geopolymer reaction. Compared to the high sintering temperatures of typical ceramic materials at 600 ºC – 1200 ºC or higher, geopolymers can be processed at temperatures close to 100 ºC, leading to a significant reduction in processing cost.

Geopolymers are an amorphous alkali aluminosilicate “inorganic polymer” produced as a result of reaction between an aluminosilicate and an alkali activator. “Geopolymerization,” the reaction to form geopolymers occurs through a series of steps. First, dissolution of aluminosilicates occurs in the presence of highly alkaline solution to form monomeric tetrahedral aluminates and silicates. These tetrahedral aluminates and silicates form polymeric Si-O-Al-O bonds, developing oligomers. Gelation occurs when the oligomers have reached a supersaturated solution. Then, polycondensation ensues as the oligomers condense and consume water in an exothermic process, forming the amorphous 3-d structure known as geopolymer [13-15]. An illustration of the geopolymerization reaction is shown in Figure 1.6.

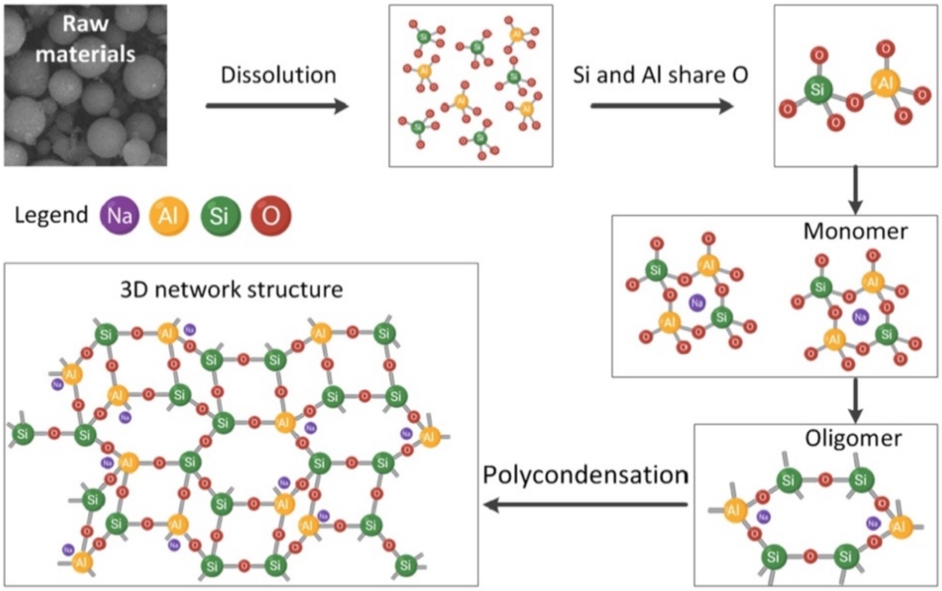

Figure 1.6 Geopolymerization steps: dissolution, gelation, and polycondensation [15].

With their high compressive strength, chemical durability, thermal durability, and low cost, geopolymers have attracted interest not just as an alternative to Portland cement [12, 15-17], but for adhesive [18-20], and coating [22-23] applications.

Monolithic and composite geopolymer membranes have been studied for a variety of wastewater treatment applications. Removal of heavy metals (Ni^{2+}, Pb^{2+}, Cu^{2+}, Cd^{2+}, and Ba^{2+}) has been shown to be successful using geopolymer materials in filtration and solution adsorption processes. [24-27]. Alcohol and water were successfully separated using a zeolite membrane that was formed by hydrothermal treatment of geopolymer [28]. Xu et al [29-30] used hydrogen peroxide foaming agent to form a porous geopolymer for removal of suspended particles in pulp-making green liquor. Porous geopolymer materials are typically formed through the addition of aluminum powder [31-34] or hydrogen peroxide [32-41] as foaming agents, or with fillers such as biochar [42-44] or zeolite [42]. Zeolites in particular have been studied for their potential for wastewater treatment [45-56].

Naveed et al [47] studied the use of fly-ash sodium-based geopolymer flat sheet membranes for the treatment of produced water in end-flow filtration. Results showed a significant reduction in turbidity and removal of suspended particles from the produced water, but with little to no reduction in conductivity and low flux due to buildup of particles on the surface of the membranes. Xu et al [42] studied the use of potassium-based geopolymer membranes using biochar and zeolite fillers. These membranes were also tested in an end-flow filtration system. Results showed that use of the zeolite filler led to improved compressive strength of the membrane and significant reduction in turbidity during produced water filtration.

CHAPTER II

OBJECTIVES

With the end goal of designing and developing a low-cost ceramic composite membrane for industrial treatment of produced water, this study explores the following two objectives:

Objective #1: Design and process self-supported geopolymer composite membranes for filtration of produced water.

In order for a ceramic membrane to be practical for industry use and adaptable in a wide variety of geometries, the membrane needs to not only be porous and structurally stable, but also be supported by a sturdy rigid scaffolding layer. This study explores the fabrication of a self-supporting geopolymer composite membrane using a perforated aluminum support layer.

Objective #2: Evaluate the performance of geopolymer composite membranes in end-flow and cross-flow filtration modes.

While end-flow filtration is ideal for lab-scale testing, cross-flow filtration is much more suited for industrial applications. The filtration performance of the self-supported geopolymer composite membrane developed in this study was tested in both end-flow and cross-flow modes to compare flux rates and water quality of the permeate.

CHAPTER III

MATERIALS AND METHODS

The materials used in this study to synthesize low-cost ceramic composite membranes are described in detail here. In addition, included here are the methods, procedures, and equipment used for synthesis, processing, and characterization (imaging, porosity, and water quality analysis.)

3.1 Materials

Ceramic composite membranes were processed using geopolymer, clinoptilolite zeolite, and perforated sheet aluminum. Geopolymer slurry was synthesized using metakaolin as the raw aluminosilicate material, mixed with alkaline solution. Zeolites were added as a porous filler material, and perforated sheet aluminum was used as a scaffolding layer to develop the self-supporting ceramic composite membrane.

3.1.1 Geopolymers

Geopolymers form through the reaction of highly alkaline solution with raw aluminosilicate materials. For this study, the reactive alkaline solution known as “waterglass” was formed using potassium hydroxide (KOH), silica fume (SiO_2) (Cab-O-Sil Fumed Silica EH-5, Cabot Corporation, Alpharetta, GA), and water. The following reaction shows the formation of potassium silicate waterglass, where “x” is the amount of water which may be varied.

$$Potassium\ hydroxide + silica\ fume + water\ \rightarrow "waterglass"$$

$$2KOH + 2SiO_2 + (x-1)H_20\ \rightarrow K_2O \bullet 2SiO_2 \bullet xH_2O$$

Metakaolin (Al_2O_3•$2SiO_2$) (Metamax, BASF, Ludwigshafen, Germany) was used as the starting raw aluminosilicate material. Formed from the anhydrous calcination of kaolin clay, metakaolin has been studied for use in geopolymer processing. In particular, one study on the encapsulation of aluminum using geopolymer reported reduced corrosion of aluminum when using Metamax as the geopolymer’s starting material [48]. The composition of Metamax obtained by XRF reported in that study is showing below in Table 3.1.

Table 3.1 Composition of Metamax metakaolin reported in literature [48].

	SiO_2	Al_2O_3	Other Oxides	Loss on Ignition	Mean Particle Size (µm)
Metamax	53.00	43.80	3.12	0.46	4.42

The below reaction shows the formation of geopolymer from potassium silicate waterglass and metakaolin:

$$Waterglass + Metakaolin \rightarrow Geopolymer$$

$$K_2O \bullet 2SiO_2 \bullet xH_2O + Al_2O_3 \bullet 2SiO_2 \rightarrow K_2O \bullet Al_2O_3 \bullet 4SiO_2 \bullet xH_2O$$

Note the amount of potassium hydroxide, silica fume, and water may be varied. Geopolymer composition ratios are commonly reported as K:Al:Si:H_2O. In the above chemical equation, the geopolymer ratio is 1:1:2:x.

Once the waterglass and aluminosilicate raw material are mixed, the geopolymer slurry is mixed with any additional fillers (zeolite in this case), and then poured into a mold or applied to a substrate material and cured under controlled temperature and humidity conditions.

For volume percent calculations of additives, the density of pure geopolymer (with no additives) was determined using a gas displacement pycnometer system, AccuPyc II 1340 (Micromeritics, Atlanta, GA) to be 2.35 g/mL. Further processing details and experimental conditions of the geopolymer composite synthesis are given later in this chapter.

3.1.2 Zeolite

Both zeolite and geopolymers are aluminosilicate materials. While chemically similar, geopolymer are amorphous while zeolites are crystalline in structure. Zeolites are commercially and widely available as adsorbents and catalysts. For this study, “fine” clinoptilolite zeolite powder was used (Clinoptilolite Zeolite 97%+ Purity, KMI Zeolite, Amargosa Valley, NV). The structure of clinoptilolite zeolite, SEM image of powder obtained, and the vendor-reported chemical analysis and properties of the clinoptilolite zeolite are listed in Figures 3.1-3.2 and Tables 3.2 – 3.3 respectively.

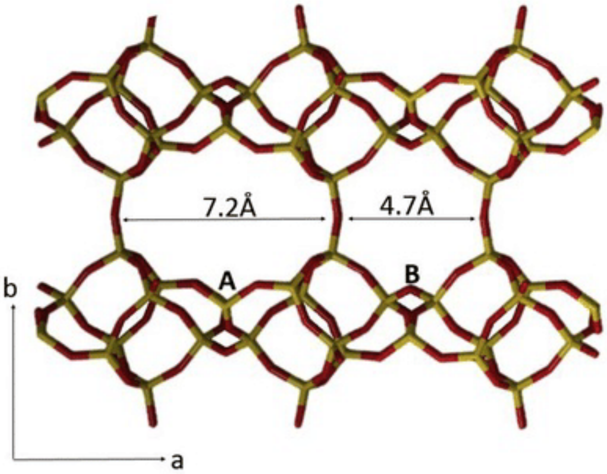

Figure 3.1 Clinoptilolite zeolite structure. Yellow lines refer to silicon or aluminum atoms, while red lines refer to covalently shared oxygen atoms. Channel opening in the zeolite structure is shown as 4.7Å-7.2Å [49].

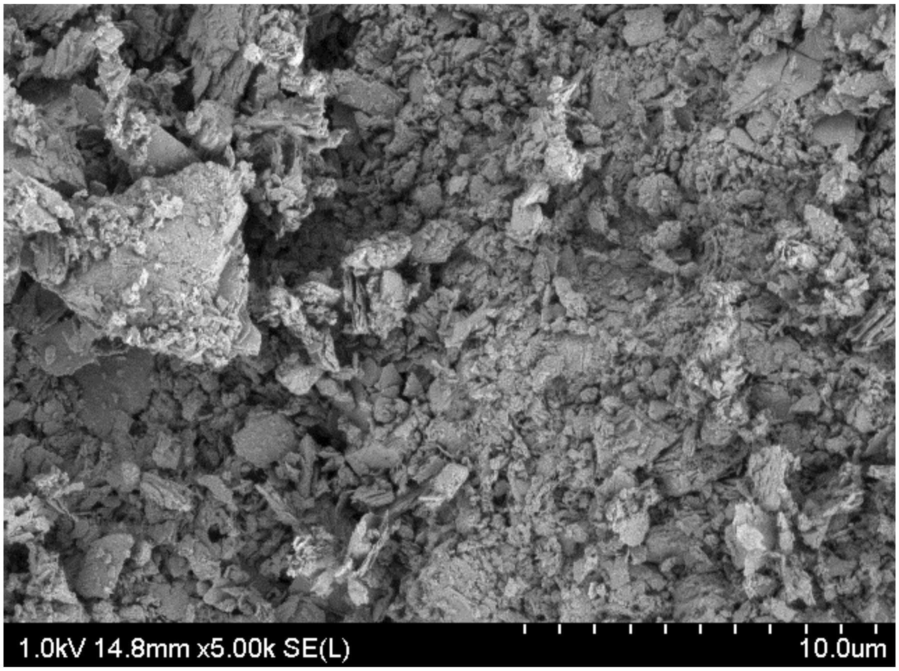

Figure 3.2 SEM Image of fine clinoptilolite zeolite powder as obtained by KMI Zeolite.

Table 3.2 Typical chemical analysis of Clinoptilolite Zeolite as reported by the vendor KMI Zeolite.

SiO_2	Al_2O_3	Fe_2O_3	CaO	MgO	Na_2O	K_2O	MnO	TiO_2
66.7%	11.48%	0.9%	1.33%	0.27%	1.80%	3.42%	0.025%	0.13%

Table 3.3 Typical property values of Clinoptilolite Zeolite as reported by the vendor KMI Zeolite.

Property	Reported Values
Chemical Formula	$Na_6[Al_6Si_{30}O_{72}]_{24}H_2O$
Clinoptilolite Content	97%+
Form	Granules and powders
Shape	Angular
Color	Beige/gray
Pore Diameter	4.0 - 7.0 angstroms
Specific Gravity	1.89
Specific Surface Area	40m^2/g
Bulk Density	45-54 lbs/ft^3
pH stability	3.0 - 10.0
Hardness	4.0 – 5.0 Mohs

Before addition to the geopolymer slurry, fine clinoptilolite powder from the vendor was sieved using a Ro-Tap RX-29 Sieve Shaker (W.S. Tyler, Ohio, USA) to obtain precise particle size ranges. Particle sizes ranging from 212 µm – 500 µm were used for geopolymer processing in this study.

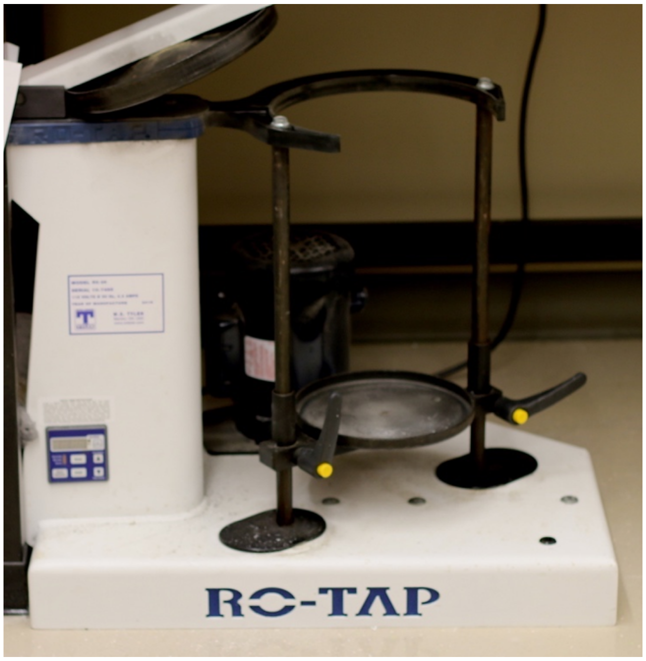

Figure 3.3 Ro-Tap RX-29 Sieve Shaker (W.S. Tyler, Ohio, USA) used to sieve zeolite powder into precise size ranges.

Table 3.4 Particles sizes of fine clinoptilolite zeolite powder, as obtained by KMI Zeolite.

US Standard Sieve #	Particle Size	Mass Percentage
	< 45 µm	0.53
#325	45 µm – 75 µm	7.60
#200	75 µm – 106 µm	11.98
#140	106 µm – 212 µm	26.40
#70	212 µm – 500 µm	38.01
#35	> 500 µm	15.18

3.1.3 Perforated Aluminum

For a self-supporting composite membrane, this study explored the use of an aluminum mesh scaffold as the support layer. Perforated aluminum 3003-h14 sheet (McMaster-Carr #MPA-17) was obtained with 0.062” round holes x 0.109” staggered area, 30% open area, and 0.032” thickness. Aluminum 3003-h14 is approximately 1.2% manganese, which increases the corrosion resistance of the metal.

The aluminum sheet was cut to the size needed, washed in 1% Alconox (Alconox Inc. White Plains, NY) in an ultrasonicator (VWR Ultrasonic Cleaner, VWR International LLC, Radnor, PA) for 15 minutes, then thoroughly rinsed and dried in a drying oven at 65ºC for at least one hour.

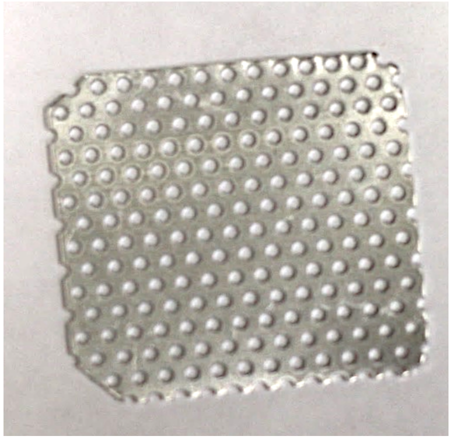

Figure 3.4 Perforated aluminum 3003-h14 with 30% open area.

Optical micrographs of the as-received aluminum mesh, shown in Figures 3.5 and 3.6, show that the surface of the aluminum is very nonuniform, both on the surface and on the edges of the mesh holes.

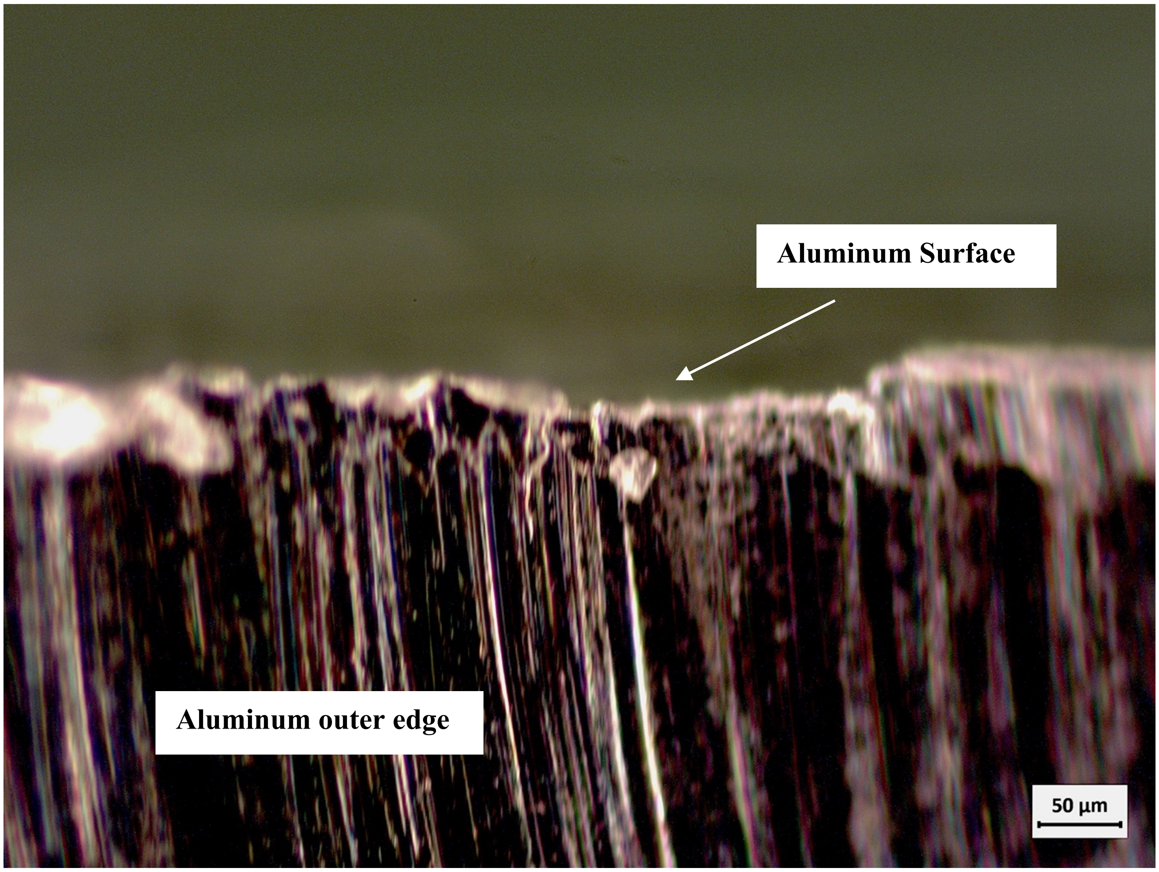

Figure 3.5 Optical micrograph of the as-received aluminum; image taken looking from a cut edge down the surface of the aluminum.

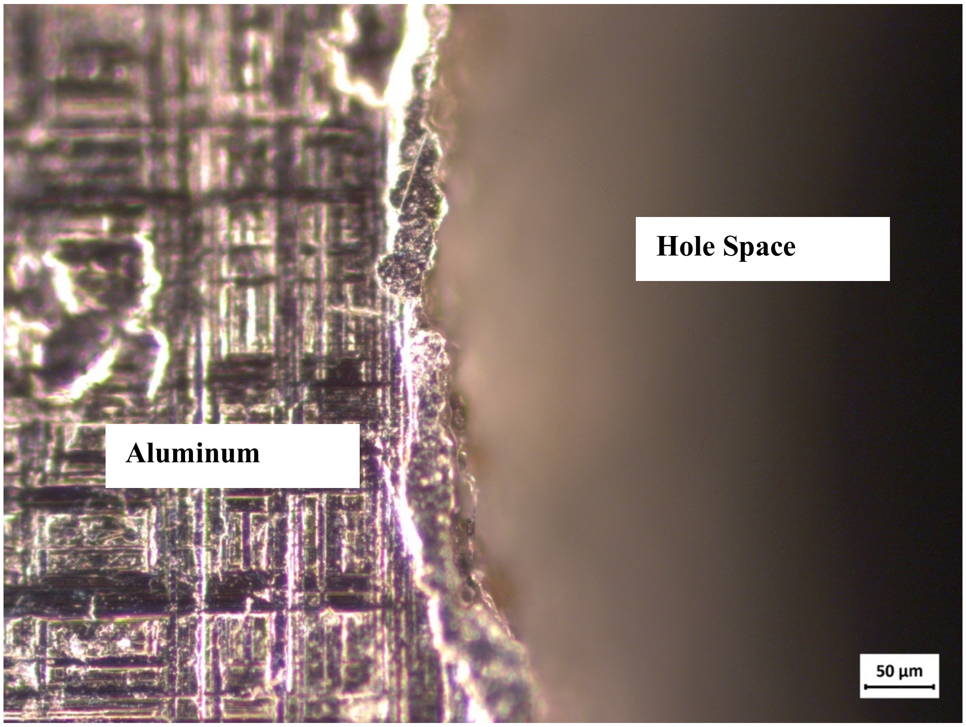

Figure 3.6 Optical micrograph of the as-received aluminum mesh. Image taken looking at the surface of the aluminum through the mesh holes.

3.2 Methods

The processing method used for the geopolymer composite structure is explained in detail here, as well as the filtration system, equipment, and flow diagrams used for testing the filtration performance of the geopolymer composite membranes. Finally, characterization methods are listed and described in detail.

3.2.1 Geopolymer Composite Synthesis

Potassium silicate aterglass was prepared by dissolving potassium hydroxide (KOH) pellets in water, and slowly adding stoichiometric amounts of silica fume (SiO_2) to form $K_2O \bullet 2SiO_2 \bullet xH_2O$. After dissolving all reactants, the solution was stirred overnight at room temperature before use in geopolymer processing.

To form the geopolymer paste, stoichiometric amounts of waterglass and metakaolin were mixed in a Thinky Mixer (ARE-310, Thinky, CA) to form $K_2O \bullet Al_2O_3 \bullet 4SiO_2 \bullet xH_2O$. The ratio of K:Al and x moles of H_20 were varied in this study to optimize the composition of the geopolymer composite for stability and adherence to the aluminum scaffold. Mixing conditions were at room temperature for 2 minutes at 500 RPM, followed by 30 seconds at 1500 RPM. Then, clinoptilolite zeolite filler was measured and added. For this study, the amount of zeolite added was varied by % volume of the total geopolymer + zeolite composite volume. The composite slurry was then mixed again in the Thinky Mixer at room temperature for an additional 2 minutes at 500 RPM and 30 seconds at 1500 RPM. After the final mixing, the geopolymer composite slurry was applied to the surface of an aluminum mesh piece cut to 1.5” square or 1.5” round depending on the type of filtration setup needed.

Figure 3.7 Thinky Mixer (ARE-310, Thinky, CA) used for mixing geopolymer slurry.

The geopolymer composite samples were placed between two pieces of flat plastic, then sealed between two pieces of weigh paper using silicone adhesive to make a sealed envelope. The samples were then clamped between two steel plates of known mass and placed in a TestEquity Controlled Temperature and Humidity Chamber (TestEquity 123H Controlled Temperature and Humidity Chamber, TestEquity, CA). Experiments were then conducted to optimize curing and drying conditions before filtration testing. An overview of the steps in geopolymer composite membrane processing is illustrated in Figure 3.8.

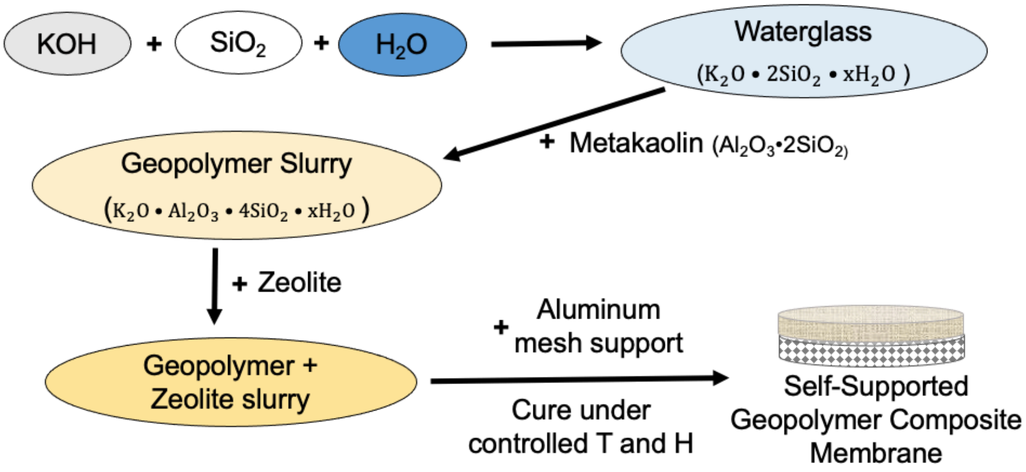

Figure 3.8 Geopolymer composite membrane synthesis process.

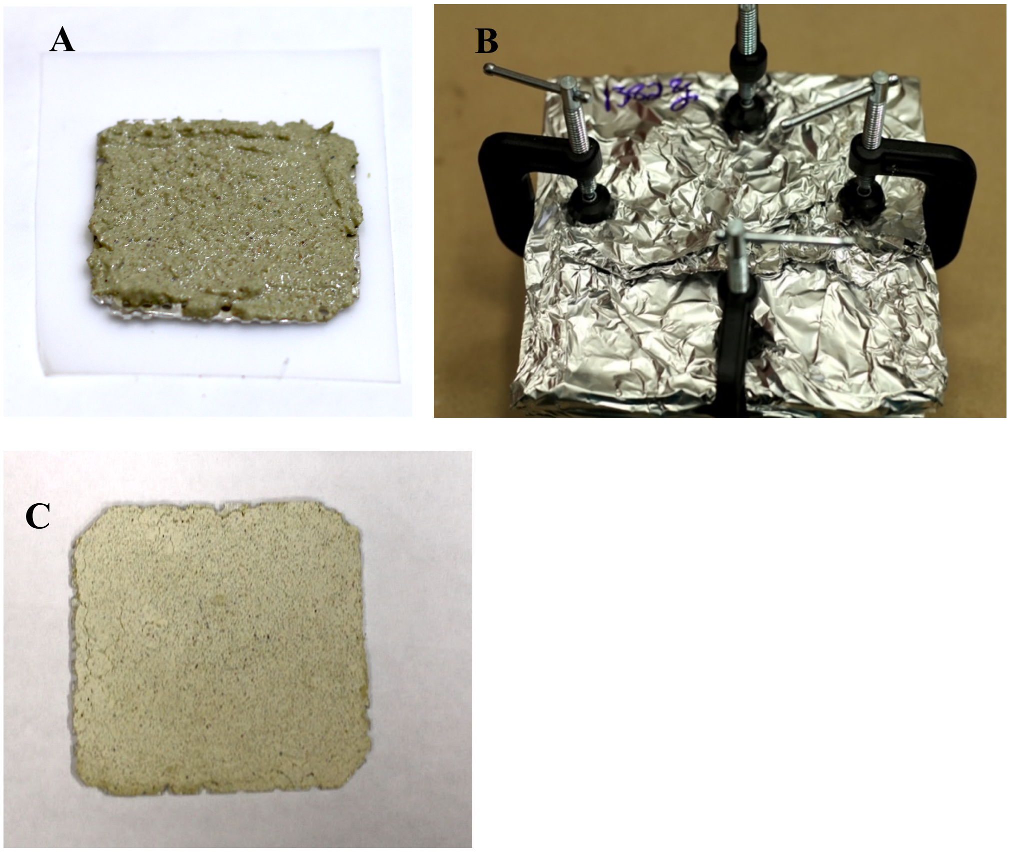

Figure 3.9 A) Wet geopolymer composite slurry on aluminum substrate, B) samples cured under applied load clamped using steel plates, C) cured and dried geopolymer composite membrane.

Figure 3.10 TestEquity Controlled Temperature and Humidity Chamber (TestEquity 123H Controlled Temperature and Humidity Chamber, TestEquity, CA) for curing geopolymer composite samples.

3.2.2 Filtration Systems

Membrane performance in end-flow filtration was tested using a previously built custom end-flow apparatus [42]. First, the geopolymer composite membrane was installed in a pipe fitting and glued using silicone adhesive to prevent water from flowing around the edges of the membrane. Then a rubber o-ring was installed on top of the membrane. The silicone adhesive was allowed to cure for 1 hour to maintain its pliability and give the rubber o-ring a flexible seat to ensure adequate sealing with the pipe fitting. The membrane was pre-wetted in distilled water, then installed into the end-flow apparatus. An image of the membrane installed in the pipe fitting is shown in Figure 3.11.

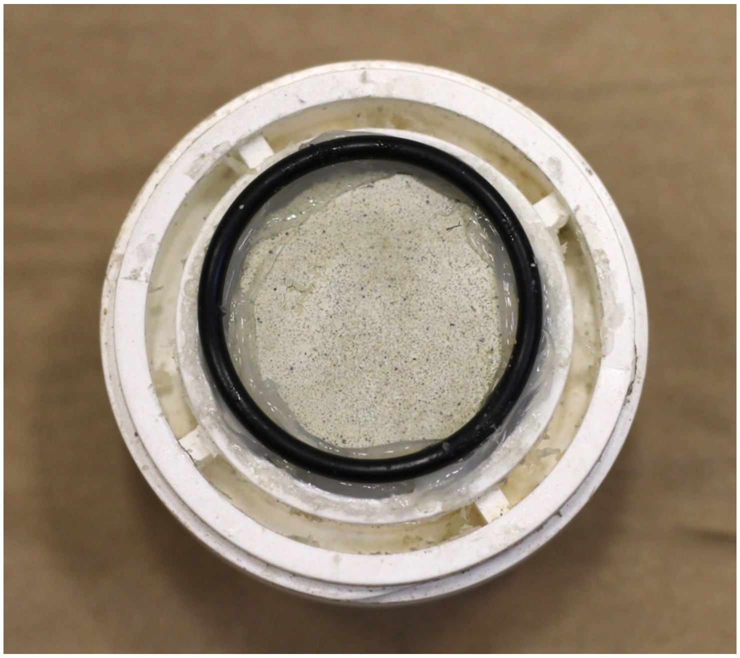

Figure 3.11 Geopolymer composite membrane installed in the end-flow apparatus pipe fitting, with the o-ring placed on the surface of the membrane.

A schematic of the end-flow apparatus is shown in Figure 3.12. After installing the membrane, valve #2 was closed while a measured quantity of 290 mL (the maximum capacity of the apparatus) produced water was poured into the top of the pipe. Afterwards valve #1 was closed and valve #2 opened, allowing pressurized air into the system. For this study, pressurized air at 30 psi and 40 psi were used to have comparable parameters of the cross-flow system that was developed. Permeate was collected at the bottom, tested for water quality, and the membrane removed. After filtration and removal of the membrane, approximately 500 mL of distilled water was poured through the end-flow apparatus to flush the system of any residual particles from the produced water.

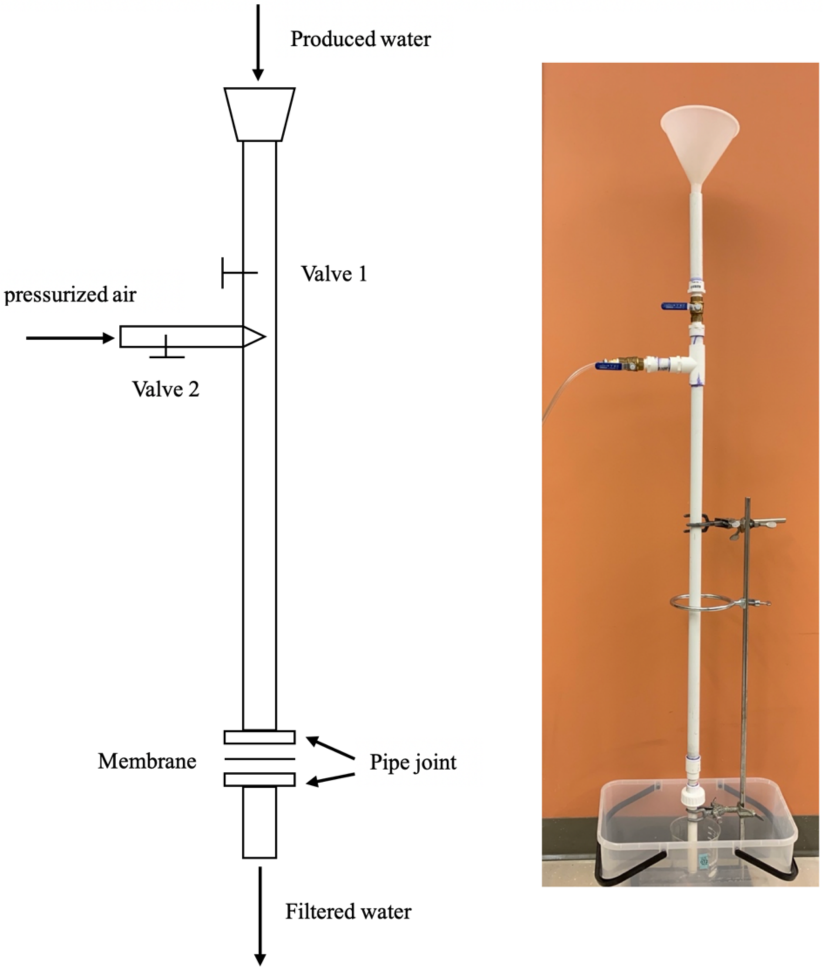

Figure 3.12 Previously built vertical end-flow apparatus used in this study [28].

Geopolymer composite membranes were tested in cross-flow filtration using a flow system that was designed for these experiments. First, the membranes were installed in a Sterlitech Cross-flow Cell (Sterlitech CF016 Cross-flow Cell, Sterlitech Corporation, WA). A schematic of the cross-flow cell is shown in Figure 3.13. The edges of the membrane were sealed with silicone adhesive and a thin bead of silicone adhesive was placed around the top of the membrane. A custom plastic spacer was glued against the membrane and the cross-flow cell to ensure an adequate seal and prevent leakage (Figure 3.14). The silicone adhesive was allowed to cure for 24 hours to ensure complete curing on the interior of the cross-flow cell . The membrane in the cross-flow cell was then pre-wetted in distilled water and installed in the cross-flow filtration system.

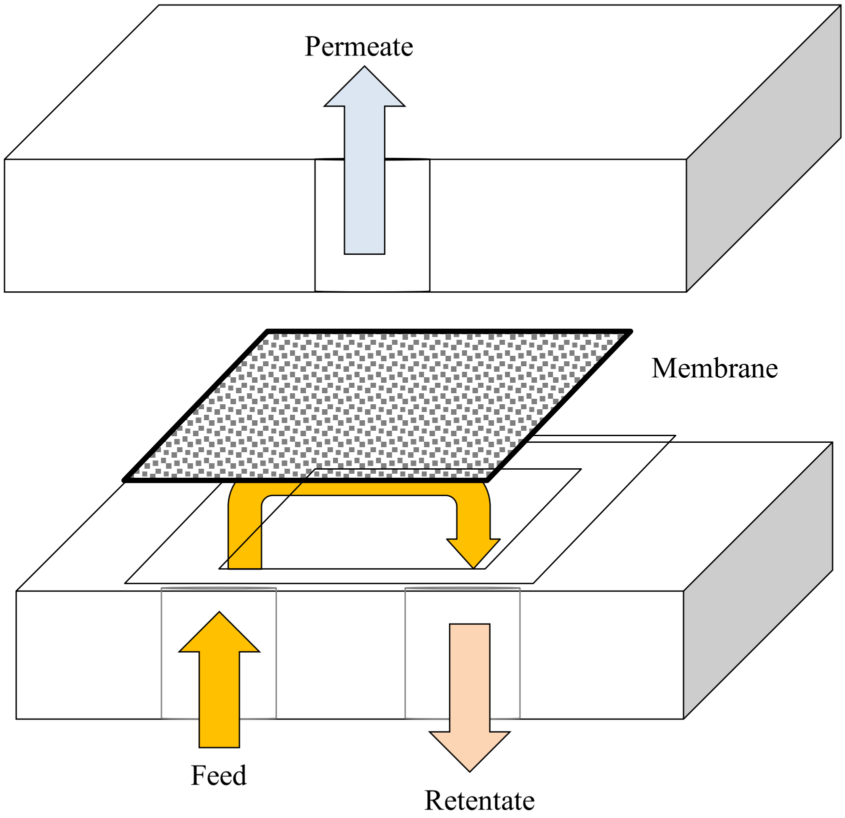

Figure 3.13 Schematic of the Sterlitech CF016 Cross-flow Cell (Sterlitech CF016 Cross-flow Cell, Sterlitech Corporation, WA) used in this study.

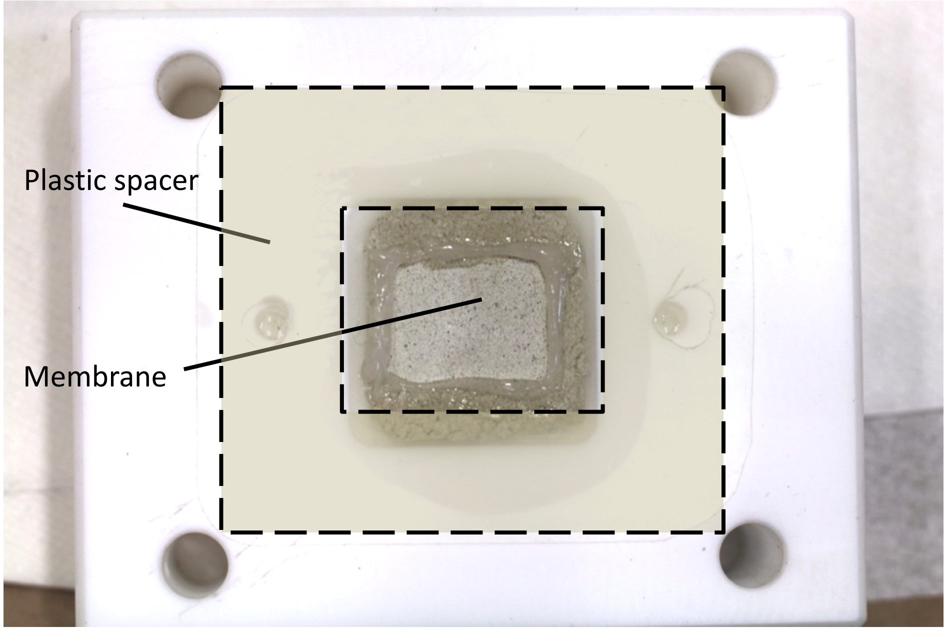

Figure 3.14 Top portion of the cross-flow cell with the geopolymer composite membrane and clear plastic spacer (shaded area) installed. The permeate port is not visible and is located behind the membrane.

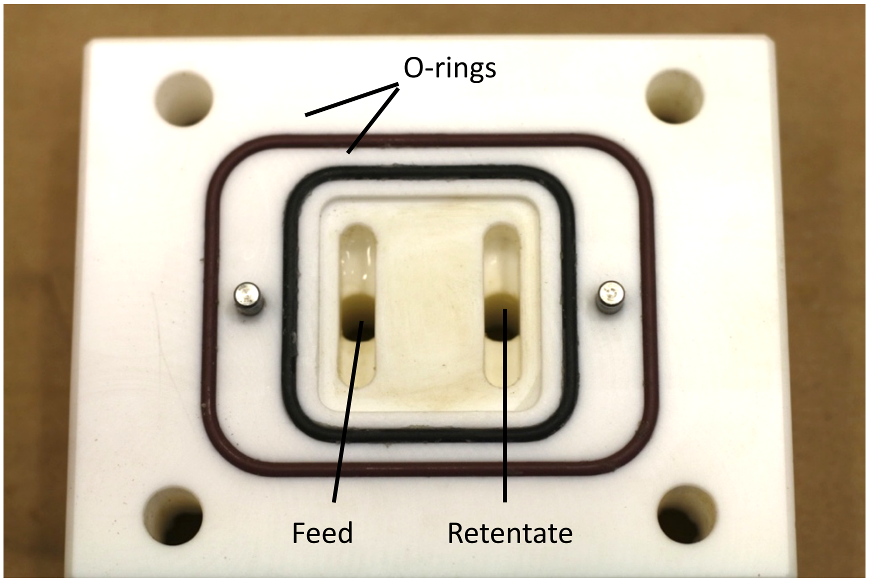

Figure 3.15 Bottom portion of the cross-flow cell showing the feed and retentate ports, as well as two o-rings that seal against the plastic spacer and prevent leakage.

A feed stream of produced water flowed from a feed tank to a Masterflex Peristaltic Pump (Masterflex L/S with EasyLoad 3 Pump Head, Masterflex, Vernon Hills, IL). The pump was operated at 75 RPM and 100 RPM; 75RPM being the minimum pump speed at which permeate began to flow, and 100 RPM being the maximum speed of the pump. The pump flow rates at 75 RPM and 100 RPM through the system without permeate flow was measured to be 0.13 L/min and 0.16 L/min respectively.

From the pump, feed water flowed to a bottom port on a Sterlitech Cross-flow Cell (Sterlitech CF016 Cross Flow Cell, Sterlitech Corporation, WA). A port at the top of the cross-flow cell allowed permeate to be collected in a permeate tank. Retentate flowed out the bottom of the cross-flow cell toward a pressure gauge and valve to control water pressure, then back to recirculate in the feed tank in a closed loop. A schematic of the custom built cross-flow system is shown in Figure 3.16.

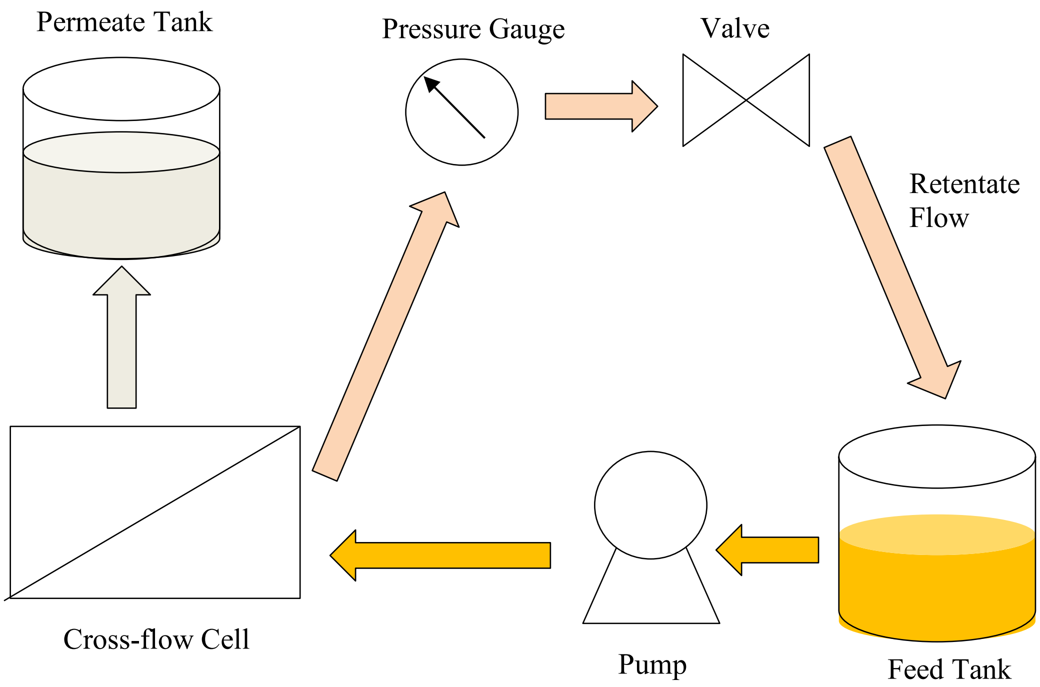

Figure 3.16 Custom built cross-flow filtration system for filtration studies of geopolymer composite membranes.

After the pre-wetted membrane was installed in the cross-flow cell, the entire system was first primed with 125 mL of distilled water. For the feed tank, a beaker of produced water was placed on a stirring plate to allow consistent solid particle concentration into the feed stream. Once produced water was introduced to the cross-flow system, the first 150mL was discarded to ensure removal of all distilled water in the system. Then the valve was adjusted to control water pressure and permeate collected in the permeate tank. Under pump speeds of 75 RPM and 100 RPM, the water pressure was adjusted to between 30 and 40 psi to have optimum permeate flow and recirculation of the retentate. Precise pressures are unable to be obtained in this system due to the nature of the peristaltic pump, which operates by applying rolling pressure to the feed tubing. After filtration, the permeate was tested for water quality and the membrane removed from the cross-flow cell. Then the cross-flow cell was reinstalled without the membrane, and a minimum of 500 mL of distilled water pumped through the system to flush it. Finally, the components of the cross-flow cell were disassembled, washed, and dried.

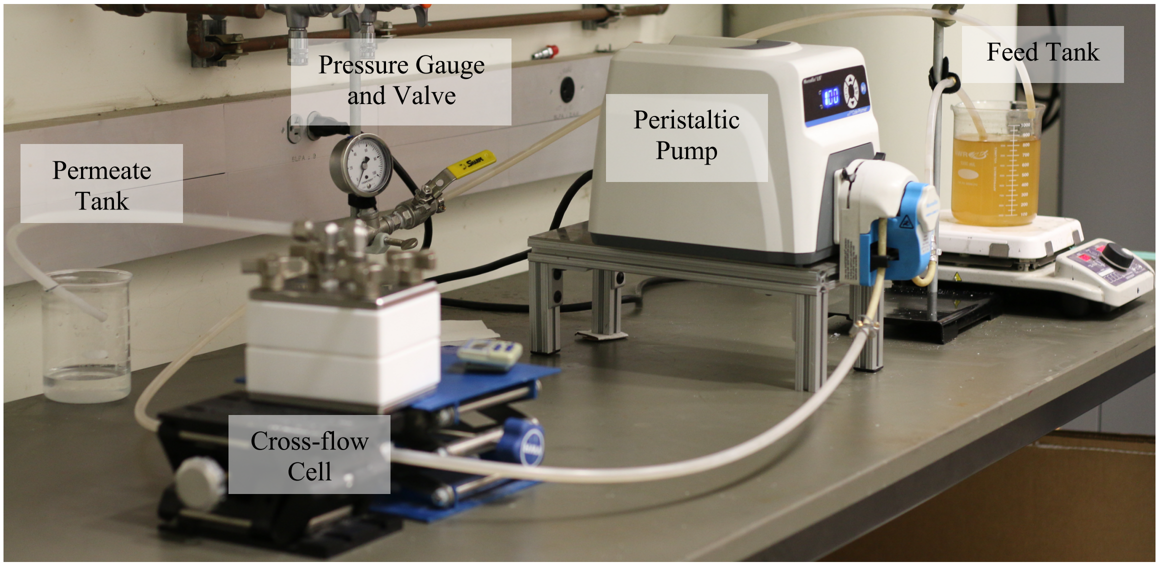

Figure 3.17 Image of the cross-flow system used in this study.

3.2.2 Imaging Analysis

Optical Microscopy

An optical microscope, Carl Zeiss' AxioLab A1 Modular upright Optical Microscope for Materials Science (Carl Zeiss Microscopy, LLC, White Plains, NY) was used with 5x, 20x, and 100x magnifying lenses to observe surface and interface of the geopolymer composite membranes.

To prepare samples for imaging the interface between the ceramic layer and the aluminum scaffold, the samples were first embedded in epoxy. Resin (Epofix Resin, Struers Inc, Cleveland, OH) was heated on a hot plate to 40ºC to reduce the viscosity and ensure the epoxy could enter the pores of the composite membrane. Then the resin was mixed with hardener (Epofix Hardener, Struers Inc, Cleveland, OH) in a 25:3 resin to hardener ratio. The samples were vacuum impregnated (Citovac, Stuers Inc., Cleveland, OH) with epoxy and allowed to cure for 18 hours. Using a slow action diamond saw (Minitom, Struers Inc., Cleveland, OH), samples were carefully cut first across the ceramic layer, then turned and cut across the aluminum layer. This was to avoid stressing the ceramic layer and causing cracks. After cutting to expose the interface between the ceramic and aluminum, the samples were embedded in epoxy a second time and then polished using Struers LaboPol-35 Polishing/Grinding System (Struers Inc, Cleveland, OH) and SiC polishing cloths. After polishing the samples were cleaned with distilled water and dried in a vacuum oven (VWR Symphony, VWR International LLC, Radnor, PA).

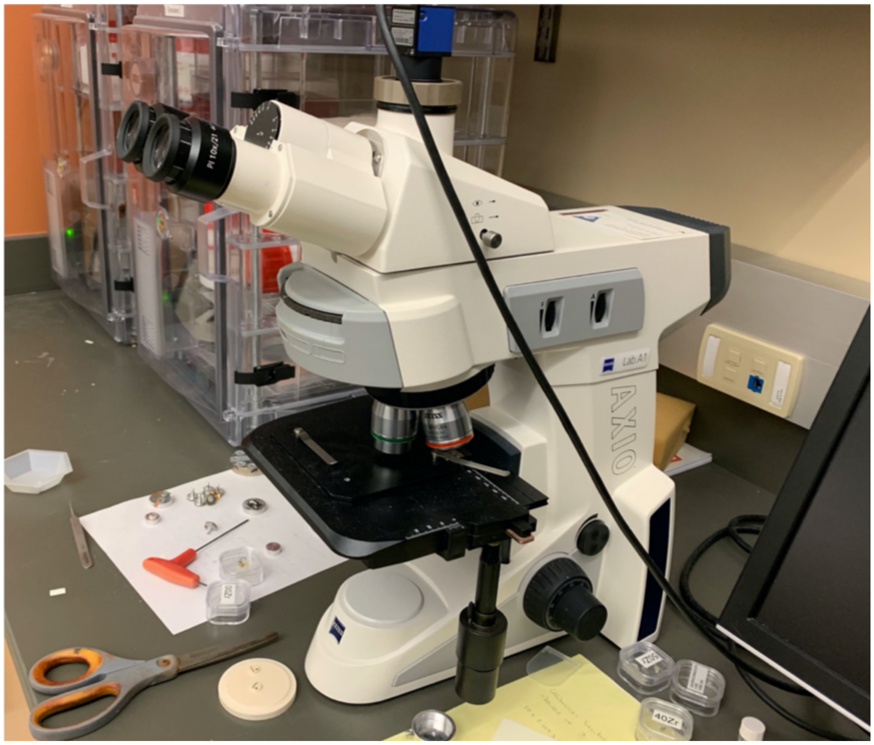

Figure 3.18 Carl Zeiss' AxioLab A1 Modular, upright Optical Microscope for Materials Science (Carl Zeiss Microscopy, LLC, White Plains, NY) used for obtaining digital images.

Scanning Electron Microscopy (SEM)

The polished samples were coated with iridium using a sputter coater (Leica EM ACE600, Leica Microsystems, Buffalo Grove, IL) for 40 seconds to prevent charging of the sample during SEM. SEM was primarily used to observe and image the interface between the ceramic layer and the aluminum scaffold at high magnifications. A Hitachi S-4800 Field Emission Scanning Electron Microscope was used for these images, along with an Oxford Instruments (Tubney Woods, Abingdon, Oxon, UK) energy dispersive (EDS) silicon drift detector to obtain elemental analysis at the interface.

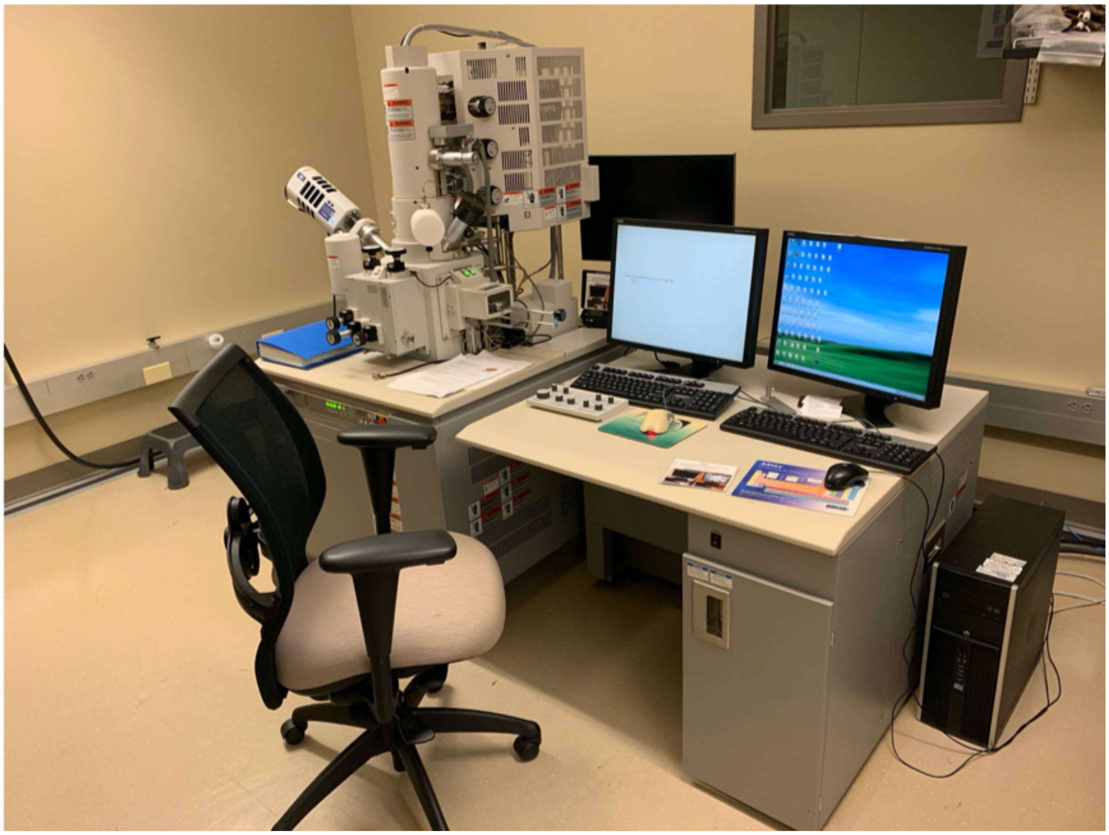

Figure 3.19 Hitachi S-4800 Field Emission Scanning Electron Microscope used for high magnification imaging in this study, coupled with an Oxford Instruments (Tubney Woods, Abingdon, Oxon, UK) energy dispersive (EDS) silicon drift detector.

Micro Computed Tomography (Micro-CT)

Micro-CT analysis was conducting using a Zeiss Xradia Vera (Carl Zeiss Microscopy, LLC, White Plains, NY) to obtain x-ray transmission images of membrane samples. After acquiring images, Avizo Software (Thermo-Scientific, Waltham, MA) was used to construct 3-d projections of the internal structure of the geopolymer composite membranes.

3.2.3 Porosity Analysis

Mercury Intrusion Porosimetry (MIP)

Mercury Intrusion Porosimetry (MIP) was used to gather information about the porous structure of the geopolymer composite membranes. An Autopore V, Mercury Intrusion Porosimeter (Micromeritics, Norcross, GA) was used for this analysis to obtain information on porosity and pore size distribution. In this analysis, samples are immersed in mercury and applied pressure is used to penetrate the pores with mercury. Based on the volume of mercury that intrudes into the samples at various pressures, the porosity data can be calculated.

Figure 3.20 Autopore V, Mercury Intrusion Porosimeter (Micromeritics, Norcross, GA) used for porosity analysis in this study.

3.2.4 Produced Water and Water Quality

Produced water from the Anadarko Shelf in Oklahoma was obtained for use in this study. The produced water was stirred prior to use for filtration testing, and water quality measured before each filtration test.

pH

The pH of the produced water was measured prior to each filtration test, and permeate water measured after filtration. A pH meter (SevenCompact pH Meter S220, Mettler-Toledo LLC, Columbus, OH) was used to analyze pH. The pH meter was calibrated regularly using standard buffer solutions according to the instrument manual. Typical drinking water pH is 7.0, acceptable agricultural water for irrigation between 5.0 and 7.0, and acceptable industrial wastewater discharge between 6.0 and 9.0.

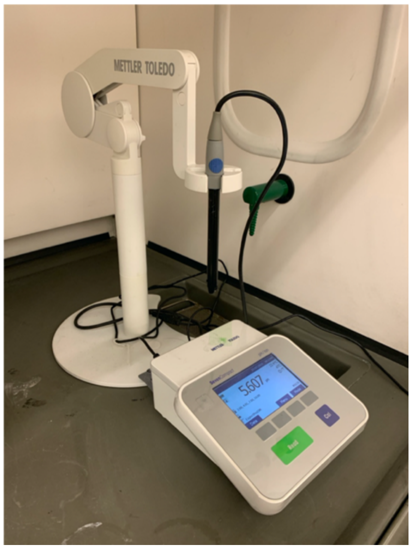

Figure 3.21 Measurements of pH were done using a SevenCompact pH Meter S220 (Mettler-Toledo LLC, Columbus, OH).

Turbidity

Turbidity refers to the clarity or haziness of a water sample due to the suspension of small particles in the water. High turbidity measurements indicate that the water contains a large amount of suspended material, which are not always visible to the naked eye. For this study, a LaMotte 1970-EPA Model 2020we Portable Turbidity Meter (LaMotte Company, Chestertown, MD) was used. The turbidity meter was calibrated daily using standard solutions according to the instrument manual. Standard turbidity readings are in nephelometric turbidity units (NTU). Typical turbidity readings are less than 1 NTU for drinking water, less than 10 NTU for agriculture, and for industrial use turbidity may vary based on the application.

Figure 3.22 LaMotte 1970-EPA Model 2020we Portable Turbidity Meter (LaMotte Company, Chestertown, MD) used to measure turbidity in this study.

Conductivity and Total Dissolved Solids (TDS)

Total dissolved solids (TDS) is a water quality measurement of the combined dissolved material in a liquid: organic, inorganic, molecular, ionized, colloidal, or suspended form. The standard definition of dissolved solids are those that can pass through a 1.5 μm glass fiber filter with no binders.

There are two main methods of determining TDS of a sample: gravimetric analysis and conductivity. Gravimetric analysis involves filtering the liquid through a 1.5 μm glass fiber filter with no binders, evaporating the liquid off, and measuring the mass of the residue remaining. This method is time consuming and prone to error with extremely high salinity solutions due to the presence of water that may be trapped in residual crystalline solids.

The conductivity method relies on the nature of dissolved ionic solids to allow water to conduct an electric current that is measurable. First, laboratory TDS measurements must be made using the gravimetric method. Then the electrical conductivity of the water is measured and correlated to the TDS measurement through a conductivity factor (k_e). Once the conductivity factor is known, further TDS measurements can be calculated from conductivity for that particular type of water sample.

$$TDS = k_e * EC$$

where TDS is the total dissolved solids measured or calculated in mg/L (ppm) and EC is the electrical conductivity measured in μS/cm at 25ºC. The correlation factor k_e varies based on the type of dissolved ionic solids due. Typical values for conductivity and k_e for various water types are listed in Table 3.5. The correlation factor is not linear with increase of dissolved solids and may be higher than 1.2 for extremely high salinity solutions such as produced water.

Table 3.5 Commonly reported values for conductivity (EC), conductivity factor (k_e), and total dissolved solids (TDS) for various water types. [49]

Water Type	EC in 25ºC (µS/cm)	k_e (TDS/EC)	TDS (ppm)
Distilled water	1 - 10	0.55 – 0.75	0.55 – 7.5
Drinking water	200 – 800	0.55	110 - 440
Freshwater	300 -800	0.55	165 - 440
Water for irrigation	500 – 3,000	0.55 – 0.75	275 - 2250
Seawater	45,000 – 60,000	0.7	31,500 – 42,000
Brine	65,000 – 85,000	0.75	48,750 – 63,750

For this study, the gravimetric method was used to determine the conductivity factor in the laboratory. A vacuum flask was setup using a 1.5 µm glass microfiber filter (Whatman 1827-110 934-AH, Global Life Science Solutions USA LLC, Marlborough, MA). Three successive 10 mL of distilled water was used to flush the filter and discarded. Then a measured amount of 100 mL of produced water was poured into the flask, filtered, and collected. The water was then dried in a drying oven at 150ºC for several days to evaporate the water and the residual mass weighed. This was compared to the conductivity measured by a conductivity meter (Oakton Con 700 Total Dissolved Solid meter, Oakton Instruments, Vernon Hills, IL), to determine the conductivity factor. The conductivity meter was calibrated regularly using standard solutions according to the instrument manual. For high conductivity solution, such as produced water, the water must first be diluted to the range of the conductivity meter and the dilution accounted for in the final result. For diluting high salinity solutions, much care must be used to dilute as little as possible to be within the range of the conductivity meter, as the more dilution used, the higher the error possible in the conductivity measurement.

Figure 3.23 Vacuum filtration setup used to measure the TDS in the laboratory and determine the conductivity factor.

Figure 3.24 Conductivity meter (Oakton Con 700 Total Dissolved Solid meter, Oakton Instruments, Vernon Hills, IL) used in this study.

CHAPTER IV

GEOPOLYMER COMPOSITE MEMBRANES

The goal of this study was to develop a low-cost self-supporting ceramic composite membrane capable of filtering produced water. To achieve this goal, a geopolymer composite membrane was developed using geopolymer with clinoptilolite zeolite filler on an aluminum mesh scaffold.

Variations in composition, filler additives, and curing conditions were explored before arriving at the optimal and final composition of the membrane.

4.1 Optimization of Composition and Curing

Composition

Depending on the type of aluminum used, literature studies have reported varying results of the bonding of geopolymer with an aluminum substrate. Corrosion of the aluminum by the alkaline geopolymer slurry has been reported as well as subsequent microcracks forming in the geopolymer matrix due to the release of hydrogen gas from the corrosion reaction [48]. In anticipation of this phenomenon, the ratio of potassium to aluminum in pure geopolymer was varied ("n" in the below geopolymer formula) from 0.8 to 1.0 and the number of moles of water ("x" in the below geopolymer formula) was varied from 11 to 16.

$$nK_2O \bullet Al_2O_3 \bullet 2SiO_2 \bullet xH_2O$$

Samples were tested with zeolite addition up to 40% volume, on aluminum supports, and the results observed. While optimizing the compositional parameters, curing was fixed under the following conditions: overnight at room temperature (20-25 ºC, 55-60% humidity), followed by curing for a minimum of 7 days at 40 ºC and 80% humidity in the TestEquity chamber.

For a 0.8 K : Al ratio with 11 moles of water, the geopolymer slurry was too thick to handle. Increasing water content to 13 or 16 moles resulted in the geopolymer not reaching fully cured status after over 14 days, as exhibited by samples being wet and soft to the touch, regardless of the presence of zeolite.

The 0.9 K : Al ratio with 11 moles of water fully cured in 12 days, regardless of the amount of zeolite. By increasing water content to 13 moles, with no zeolite the samples cured in the 7 days minimum curing time, but cracks appeared on the surface of the membranes and the geopolymer composite peeled off the aluminum support when pulled by hand. With the addition of 20% vol zeolite, the samples exhibited less surface cracking, but still peeled away from the aluminum support. By increasing zeolite content to 40% vol, the samples continued to cure in 7 days, but showed even further reduced surface cracking while appearing to adhere to the aluminum support. Increasing water content to 16 moles of water resulted in the samples not reaching a fully cured state, even after 14 days.

With a 1.0 K : Al ratio with 11 moles of water and no zeolite addition, samples fully cured in the 7 day minimum curing time, adhered well to the aluminum support, but showed surface cracks.

Similar to the trend seen with the 0.9 K : Al samples, increasing the amount of zeolite addition resulted in few and few surface cracks. With 40% vol zeolite, the 1.0 K : Al samples showed no surface cracking and good adherence to the aluminum. Unfortunately, after curing and removal to room temperature, the samples cracked within 1 hour. Increasing water content to 13 or 16 moles resulted in a slurry too thin to handle.

Milled glass fibers of length 16 μm (Microglass 7232, Fibertec Inc, Bridgewater, MA) were also added to see the effect on the structure of the membrane. Experimental observations were that the addition of 1% - 3% wt of the milled glass fibers did not have an effect on the surface cracking of the samples but increased rate of the hardening of the geopolymer slurry which reduced its workability.

Therefore, the 1.0 K : Al ratio with 11 moles of water and the addition of 40% vol zeolite was found to be the optimum composition for the geopolymer composite membranes, shown as the row shaded green in Table 4.1. The occurrence of surface cracking after removal to room temperature was then addressed with optimization of the curing conditions.

Table 4.1 Comparison of compositional variables and experimental observations.

K:Al Ratio	**X moles Water**	**Zeolite (% vol)**	**Curing @ 40ºC (minimum 7 days)**	**Surface Cracks**	**Adherence to Aluminum**
0.8	11	0 – 40%	Slurry too thick to handle	N/A	N/A
0.8	13 – 16	0 – 40%	14+ days	N/A	N/A
0.9	11	0 – 40%	12 days	N/A	N/A
0.9	13	0%	7 days	Cracks	Peeled Off
0.9	13	20%	7 days	Some Cracks	Peeled Off
0.9	13	40%	7 days	Few Cracks	Intact
0.9	16	0 – 40%	14+ days	N/A	N/A
1.0	11	0%	7 days	Cracks	Intact
1.0	11	20%	7 days	Some Cracks	Intact
1.0	11	40%	7 days	Cracks after removal to room temp	Intact
1.0	13 – 16	0 – 40%	Slurry too thin to handle	N/A	N/A

Curing Conditions

To minimize cracking and obtain thin and uniform membranes, steel plates of known weights were used to apply compressive load on the samples during curing. The loads ranged from 4.95 g/cm^2 to 7.62 g/cm^{2,} and thickness of the final composite membrane was measured using a digital micrometer. The thickness included the thickness of the aluminum mesh support, as will be discussed in a later section. There did not appear to be a significant correlation between the applied load and the thickness of the membranes for the selected range of loads. It is anticipated that increasing the loads will reduce the thickness of the membranes, but this was not explored in this study.

Table 4.2 Observed samples thicknesses under varying loads.

Load (g/cm^2)	Approximate Thickness (mm)	Error (mm)
4.95	2.381	±0.135
5.04	2.147	±0.140
5.72	2.185	±0.079
7.20	2.222	±0.108
7.62	2.195	±0.062

Geopolymer slurry is typically cured at conditions ranging from 40 ºC to 80 ºC with humidity ranging from 40% to 80% relative humidity. In this study, the TestEquity chamber was used to control soaking and ramping temperatures and humidity for all curing experiments. Composition was fixed using the optimized parameters discussed previously, and humidity was fixed at 80%. Curing temperature and time was then optimized for full curing, reduction of surface cracks, and minimal curing time.

Samples discussed previously were cured overnight at room temperature, followed by soaking at 40 ºC for 7 days, and exhibited surface cracking within 1 hour after curing and removal to room temperature. First, soaking time was reduced to 4 days and the temperature varied between 40 ºC and 80 ºC to see the impact. After 4 days at 40 ºC, samples were not fully cured. Increasing temperature to 60 ºC, samples once again experienced surface cracking after removal to room temperature. Increasing temperature further to 80 ºC, samples experienced a large amount of surface cracking during curing.

To address the cracking after curing and removal to room temperature, a ramping step was added from room temperature to soaking temperature and a second ramping step was added from soaking temperature back down to room temperature to reduce any thermal expansion mismatch between the geopolymer composite and the aluminum support. The initial experiment used a ramping step from 20 ºC to 40 ºC over 8 hours, soaking at 40 ºC for 4 days, and then a ramping step down to 20 ºC over 10 hours. Results showed that this process still did not have enough total curing time and temperature to ensure full curing of the samples. A similar curing process was completed using 60 ºC as the soaking temperature: 20 ºC to 60 ºC over 8 hours, 60 ºC for 4 days, and 60 ºC to 20 ºC over 10 hours. The samples showed no visible surface cracks after removal to room temperature.

From here, the curing condition was optimized to reduce curing time even further. First, the initial ramping step to soaking temperature was removed, and samples were placed immediately in the TestEquity chamber for soaking at 60 ºC for 4 days. After ramping back to 20 ºC over 10 hours, the samples continued to show intact surface after removal to room temperature. Then, the ramping step down was reduced to 5 hours instead of 10 hours, with continued intact results. Finally, the soaking time was reduced from 4 days to 36 hours while maintaining intact surface of the membrane. Samples cured in less than 36 hours were found to not be fully cured. A summary of the optimization of the curing temperature and time is shown in Table 4.3.

Table 4.3 Optimum curing conditions for geopolymer composite membranes.

Step 1: Room Temperature	**Step 2: Soaking Temperature**	**Step 3: Ramp to Room Temperature**	**Observations**
Overnight in lab	40 ºC, 7 days		Cracked after removal to room temp
Overnight in lab	**40 ºC**, 4 days		Not fully cured
Overnight in lab	**60 ºC**, 4 days		Cracked after removal to room temp
Overnight in lab	**80 ºC**, 4 days		Many cracks throughout
Ramp 20ºC to 40ºC over 8 hours	40 ºC, 4 days	**Ramp down to 20ºC over 10 hours**	Not fully cured
Ramp 20ºC to 60ºC over 8 hours	**60 ºC, 4 days**	Ramp down to 20ºC over 10 hours	No visible cracks after removal to room temp
N/A	60 ºC, 4 days	Ramp down to 20ºC over 10 hours	No visible cracks after removal to room temp
N/A	60 ºC, 4 days	Ramp down to 20ºC over **5 hours**	No visible cracks after removal to room temp
N/A	60 ºC, **36 hours**	Ramp down to 20ºC over 5 hours	No visible cracks after removal to room temp
N/A	60 ºC, **< 36 hours**	Ramp down to 20ºC over 5 hours	Not fully cured

After full curing and removal to room temperature, it was noticed that the sample surfaces were slightly wet and deteriorated when introduced to water with 7 days after curing. Due to this observation, additional optimization of the curing conditions was needed. For this optimization step, the curing temperature and times were fixed at the final values discussed above, and the humidity was varied.

The previous curing experiments were done at 80% humidity. Initially, humidity was dropped t 0% and the samples cured in a drying oven. As expected, due to geopolymerization consuming water during the curing phase, the samples exhibited numerous surface cracks. Humidity was then increased to 40%; once again, sample surfaces deteriorated when exposed to water after curing. Then it was noticed that if samples were allowed to dry at room temperature for 24 hours, the samples remained intact when exposed to water. A summary of the optimization of the humidity conditions is shown in green in Table 4.4.

Table 4.4 Optimization of curing humidity.

Humidity	Additional Drying	Observations
80%	N/A	Deteriorated when exposed to water within first 7 days
0% (drying oven)	N/A	Some surface cracks
40%	N/A	When immediately removed, deteriorated in water
40%	24 hours in lab	Intact when exposed to water

The final optimized curing conditions for the geopolymer composite membranes are summarized in the below table.

Table 4.5 Optimum curing conditions for geopolymer composite membranes.

Step	**Temperature**	**Humidity**	**Curing Time**
1	60 ºC	40%	36 hours
2	60 ºC ramp to 20 ºC	40%	5 hours
3	Room temperature	Indoor humidity	24 hours

4.2 Characterization and Microstructure

Final geopolymer composite membranes were circular with 1.5” diameter or end-flow filtration testing and 1.5” square for cross-flow filtration testing. The perforated aluminum scaffold was cut to the shape needed, which determined the final shape of the overall membrane. An optical micrograph of the surface of the geopolymer composite membranes is shown in Figure 4.2. Zeolite particles are clearly visible embedded in the geopolymer matrix.

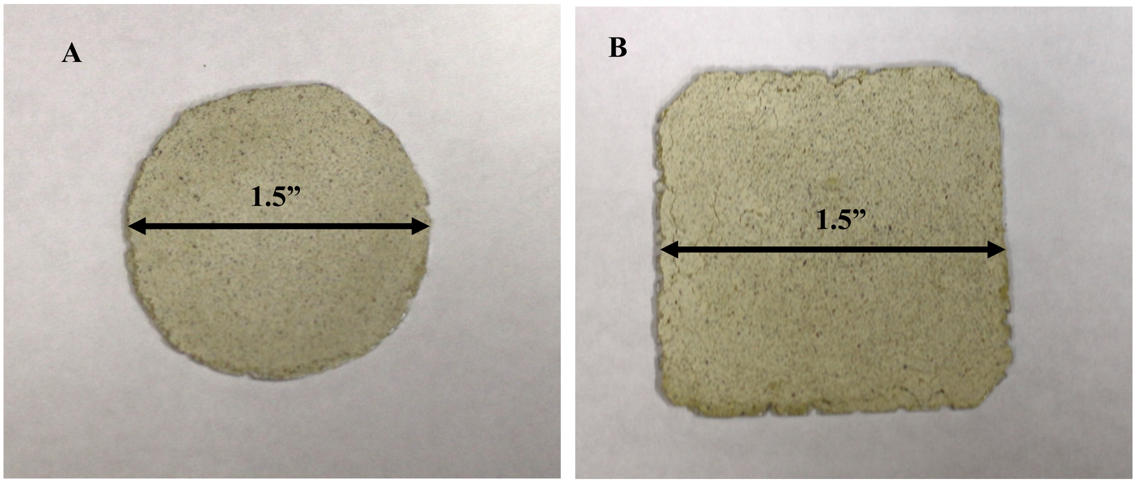

Figure 4.1 Geopolymer composite membranes prepared for A) end-flow filtration, and B) cross-flow filtration.

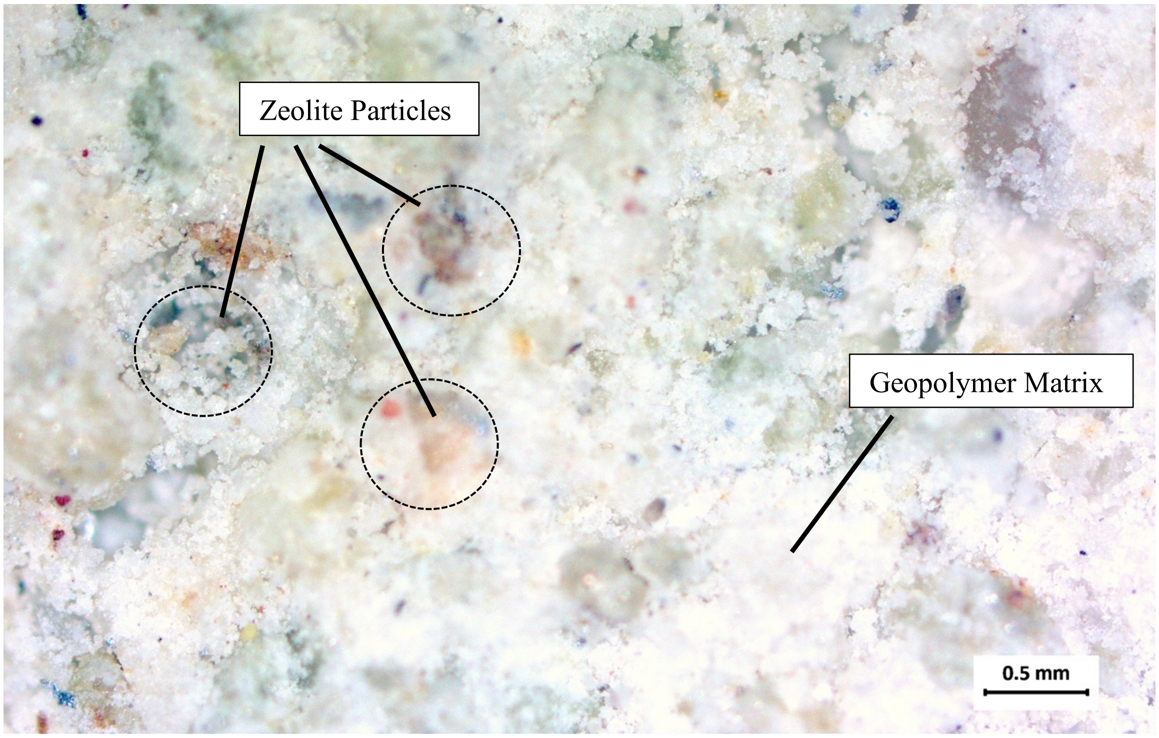

Figure 4.2 Optical micrograph of the unpolished surface of the geopolymer composite membrane, showing zeolite particles embedded in the geopolymer matrix.

Following the procedure detailed in the previous chapter, membrane samples were embedded in epoxy, cut, and polished to observe the interface between the ceramic layer and the aluminum layer. When viewed with an optical microscope, larges pores, microcracks or microchannels, and zeolite particles are visible (Figure 4.3). The interface between the zeolite particles and the geopolymer matrix was seamless.

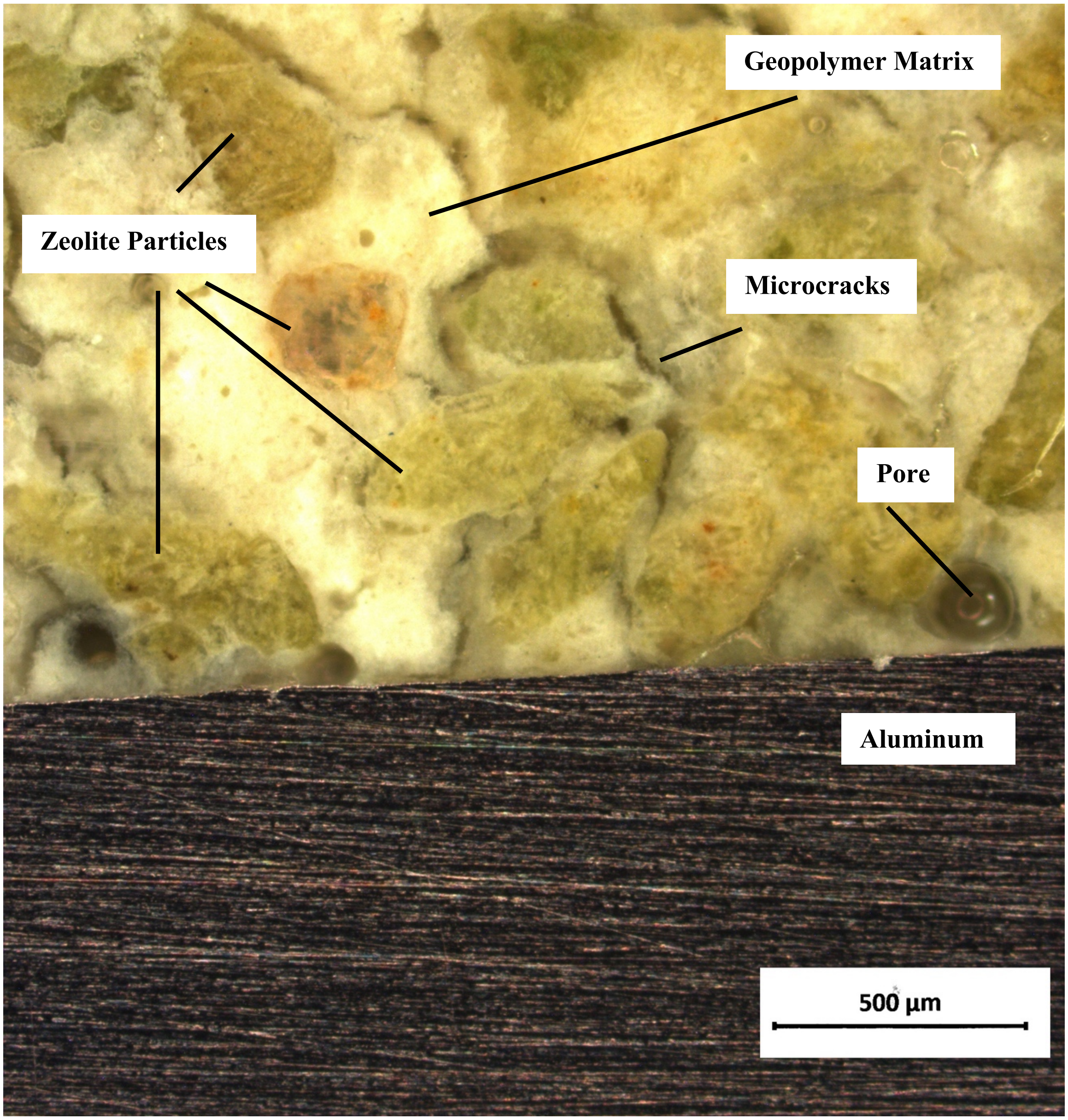

Figure 4.3 Optical image of the interface between the ceramic layer and aluminum layer.

When viewed at low magnifications, the ceramic layer is clearly seen to occupy the space in the holes of the aluminum mesh (Figure 4.4 and Figure 4.5) and some large pores and microcracks or microchannels are also visible. Since the aluminum mesh contained 30% open area and the geopolymer composite was clearly present in the holes of the mesh, the membrane area used for flux calculations was 30% of the surface area of the samples. The total thickness of the membrane reported earlier included the aluminum support since the geopolymer occupied the holes of the mesh.

Figure 4.4 Optical micrograph of the cross-section of a geopolymer composite membrane showing the presence of geopolymer matrix and zeolite particles in the holes of the aluminum mesh support.

In Figure 4.5 is very difficult to distinguish the zeolite particles from the geopolymer matrix in SEM, again confirming that the zeolite and geopolymer were bonded seamlessly. Multiple microchannels are also visible in the SEM image.

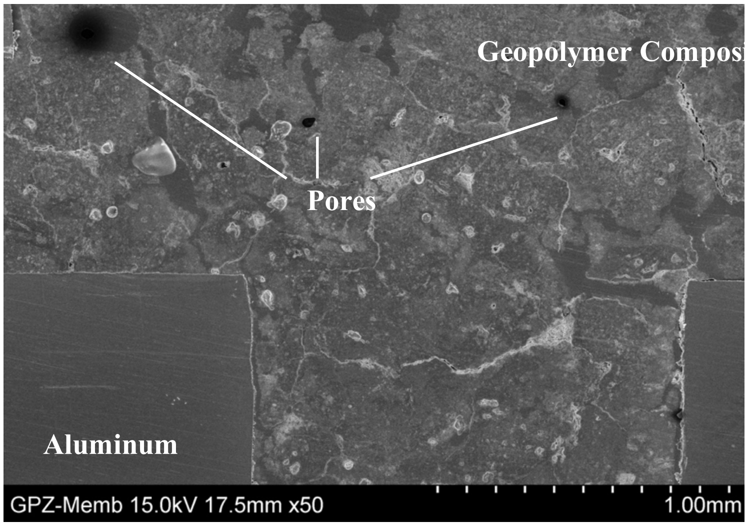

Figure 4.5 SEM image of the interface between the ceramic layer and the aluminum layer at 50x magnification, showing the geopolymer occupying the space in the aluminum holes.

A 3-d MicroCT image was taken of the geopolymer composite samples. The composite is again clearly seen to occupy the hole space of the aluminum mesh.

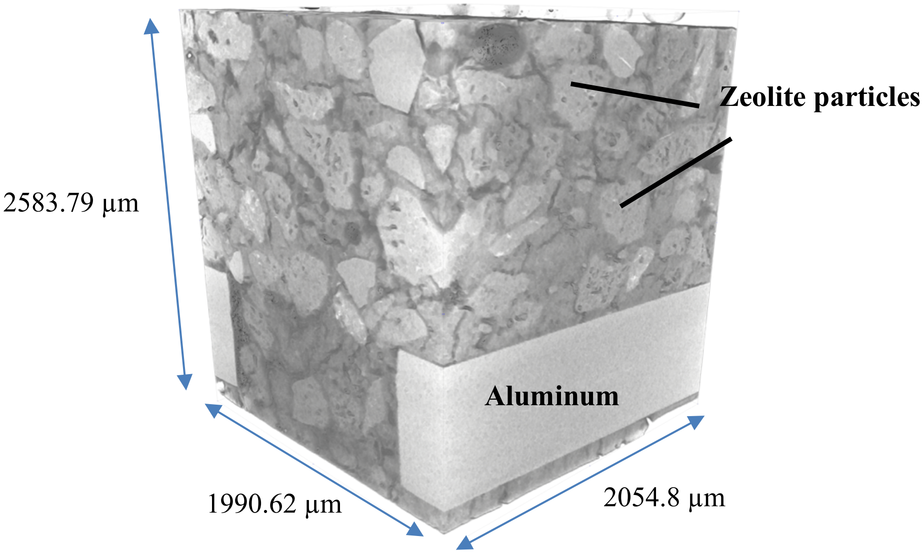

Figure 4.6 Micro-CT image of the geopolymer composite membrane.

Although large pores are visible in the SEM image, for precise measurement of pore size, pore size distribution, and porosity of the membranes, mercury intrusion porosimetry (MIP) was used. A plot of the incremental pore volume vs pore diameter in Figure 4.7 gives a graphical image of the pore size distribution. The minimum pore size detected in the membranes was found to be approximately 0.480 µm, which puts the geopolymer composite membranes in the microfiltration or particle filtration regime. MIP analysis also determined that the samples had 24.3% porosity, indicating a relatively large amount of pores within the membrane. The permeability was determined to be 4,083 mdarcy, indicating a permeable membrane with relatively well-connected pore and microchannels. Finally, the tortuosity of the membranes was found to be 5.6124. Tortuosity is a measure of the length of a microchannel if it was straight compared to the actual length. Therefore, a tortuosity of 5.6124 indicates that the membranes have very curvy microchannels, as was expected.

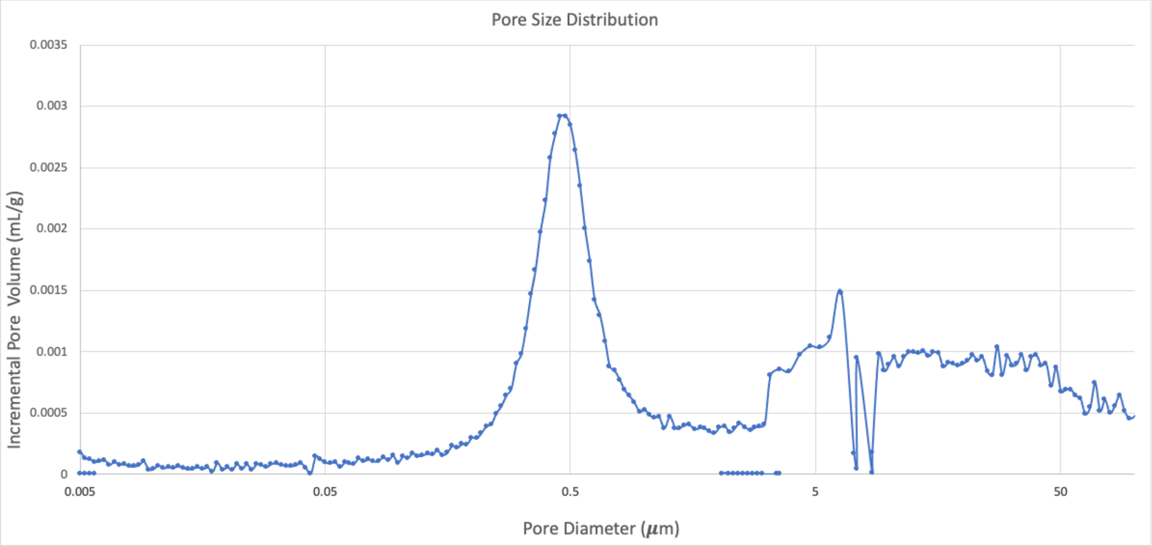

Figure 4.7 MIP data showing pore size distribution. Minimum pore size detected for the membranes was approximately 0.480 µm.

CHAPTER V

MEMBRANE PERFORMANCE

The goal of this study was to develop a low-cost self-supporting ceramic composite membrane for the filtration of produced water. Overall filtration results were favorable as seen in Figure 5.1.

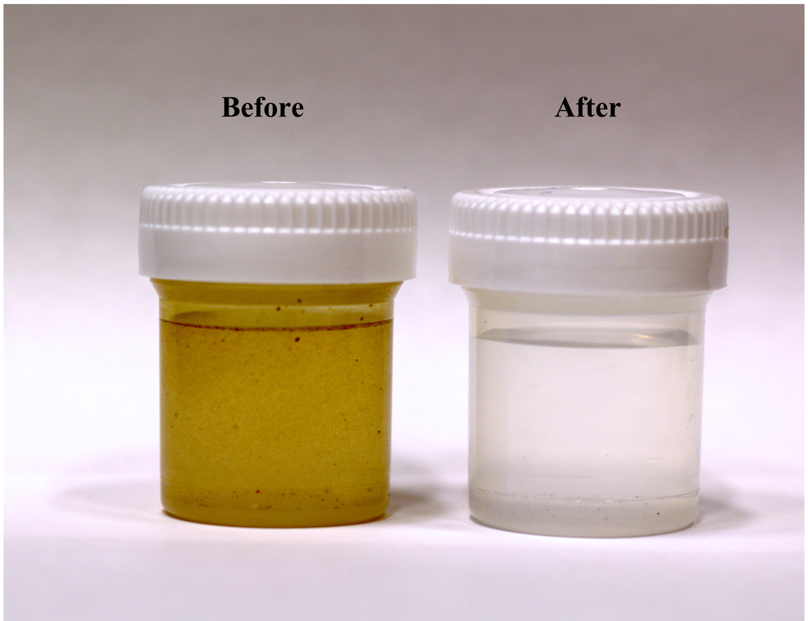

Figure 5.1 Produced water before and after filtration with the geopolymer composite membrane. The permeate sample shown here was from cross-flow filtration at 100 RPM.

Before and after filtration of each sample, water quality characteristics were measured for the produced water and permeate. The pH, conductivity, and turbidity were measured using the methods outlined in Chapter 3. For TDS measurements, results from the gravimetric experiment showed a conductivity factor of 1.3. Notably, the TDS measurements correlate well with the reported TDS of Anadarko produced water [51].

5.1 End-flow Filtration Results

Images of the geopolymer composite membrane are shown below for before and after filtration with the end-flow apparatus. Note that this image was taken after the membrane had dried, so the crystallization of the collected solids on the surface are apparent.

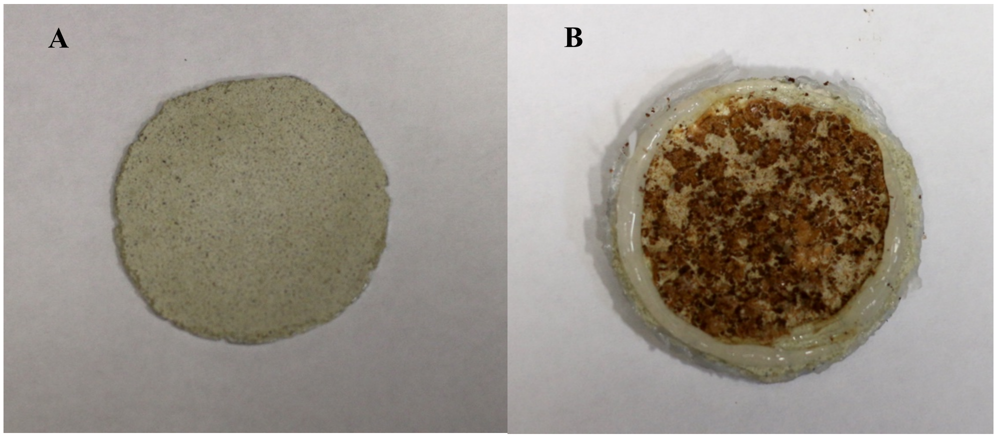

Figure 5.2 Geopolymer composite membrane before (A) and after (B) end-flow filtration.

Water quality results for end-flow filtration are shown in Table 5.1. The results showed an increase in pH, most likely due to unreacted alkaline solution in the geopolymer, and was slightly higher than that of drinking water (7.0) or agricultural water (5.0-7.0). The turbidity of produced water was reduced by 77% - 79%, but was still higher than that needed for agricultural water (less than 10 NTU). The extremely high conductivity and TDS values of produced water experienced very little reduction, indicating that the geopolymer composite membranes were not removing dissolved solids as well as that of the suspended particles. This result logically follows from the relatively large pore size of the membranes; these membranes are in the microfiltration or particle filtration regime and would need much smaller pore sizes to reach the ultrafiltration or nanofiltration regime to remove dissolved solids.

Table 5.1 Water quality results for end-flow filtration.

Sample	**pH**	**Turbidity (NTU)**	**Conductivity (µS/cm)**	**TDS (ppm)**
Produced Water	6.78	60.6	145,100	188,630
30 PSI Permeate	7.41	14.2	116,200	151,060
Produced Water	6.92	73.3	205,300	266,890
40 PSI Permeate	7.53	15.3	182,600	237,380

5.2 Cross-flow Filtration Results

Images of the geopolymer composite membranes before and after cross-flow filtration are shown in Figure 5.3. Similar to the end-flow, solid particles are visibly collected on the surface of the membranes.

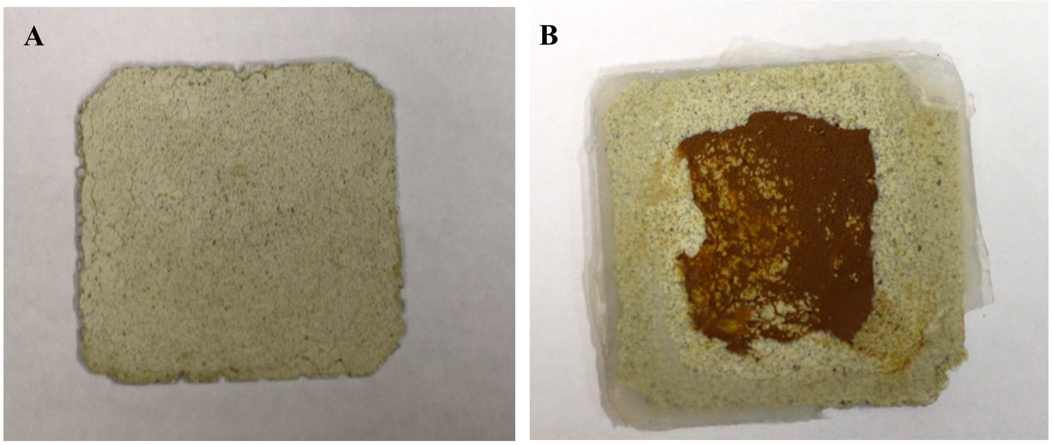

Figure 5.3 Images of the geopolymer composite membrane before and after cross-flow filtration.

Water quality results for cross-flow filtration are summarized in Table 5.2. Similar to the end-flow filtration results, the pH increased, again possibly due to any unreacted alkaline solution in the geopolymer. Under 75 RPM, the turbidity dropped approximately similar to the end-flow filtration results. However under 100 RPM, the turbidity dropped 89% to be on average 6.8 NTU which is within the limit for agricultural use. The conductivity and TDS were reduced similarly as the results in end-flow filtration, showing the membrane once again did not significantly remove the dissolved solids from the produced water.

As 75 RPM was the minimum pump speed that permeate flow was achieved with the cross-flow setup, the similar turbidity results as end-flow show that under low pump speeds and subsequent low water flow, the membrane experienced similar filtration action as end-flow. This is likely due to inadequate water flow to carry away caking particles in the retentate flow, and instead the water pressure pressing the particles against the membrane surface as in end-flow. At 100 RPM (the maximum speed of the pump), the cross-flow process was likely more fully enacted with the water pressure carrying away particles in the retentate rather than pressing the particles against the membrane surface.

Table 5.2 Water quality results for cross-flow filtration.

Sample	pH	Turbidity (NTU)	Conductivity (µS/cm)	TDS (ppm)
Produced Water	6.80	61.4	140,000	182,000
75 RPM Permeate	7.20	14.1	113,900	148,070
Produced Water	6.91	58.9	144,300	187,590
100 RPM Permeate	7.35	6.8	137,090	178,217

Although the results showed up to 89% reduction in turbidity, it was expected to have nearly 100% reduction in turbidity with microfiltration using the membranes' 0.480 µm pore size. It was suspected that corrosion of the aluminum layer at the interface with the alkaline geopolymer slurry had caused cracking or debonding at the interface, resulting in large channels for water flow without filtration.

An SEM image taken at 200x magnification in Figure 5.4 indeed shows apparent debonding or cracking near the interface. A close-up of the interface is given at 1,000x magnification in Figure 5.5. To confirm that the crack is at the interface and not within the geopolymer or within the aluminum, an EDS elemental analysis line scan was done. As expected, the debonding was confirmed to be between the geopolymer composite (high in Si and Al) and the aluminum support (high in Al only) (Figure 5.6), most likely due to corrosion of the aluminum.

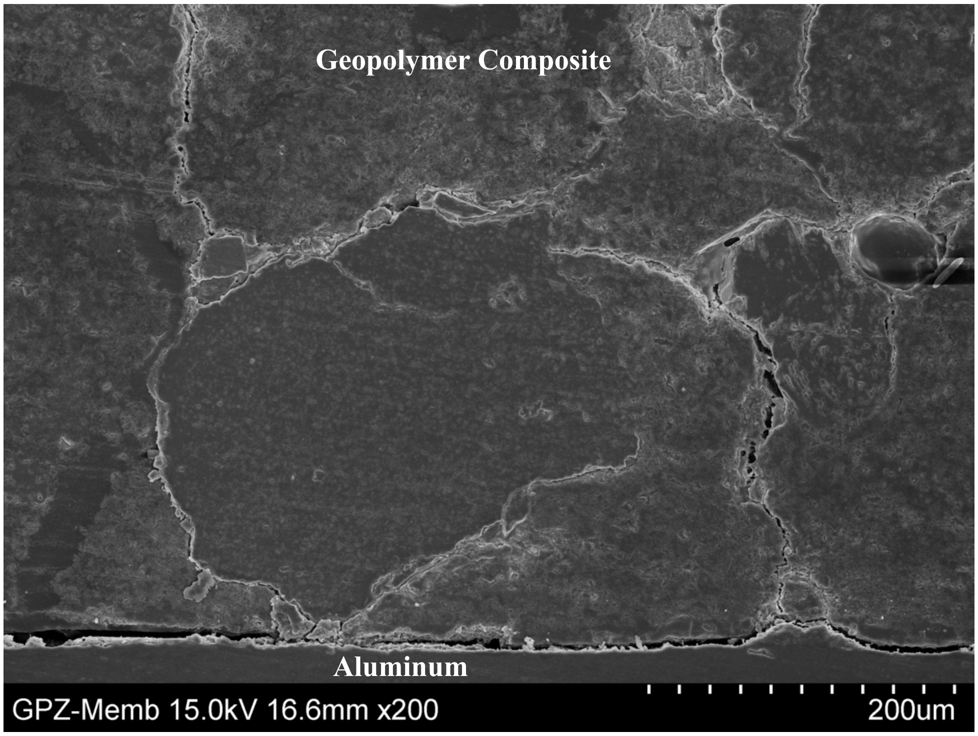

Figure 5.4 SEM image of the interface at 200x magnification.

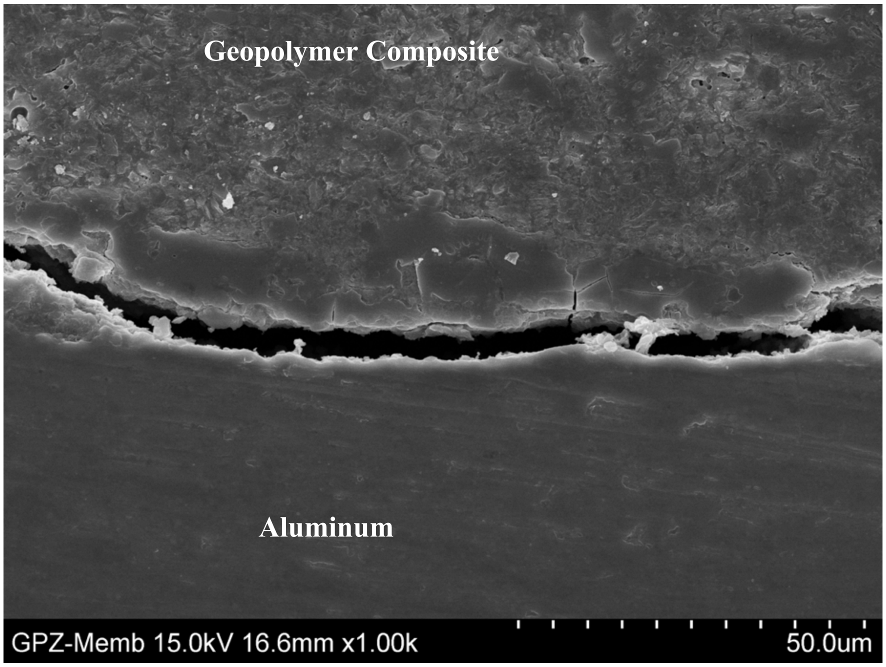

Figure 5.5 SEM image at 1,000x magnification clearly shows debonding or a crack at the interface.

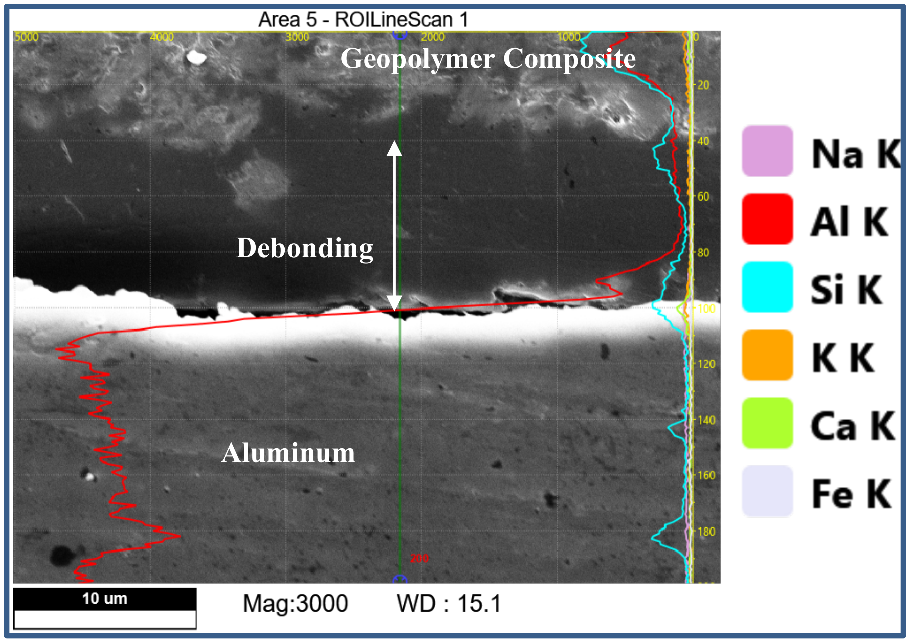

Figure 5.6 EDS elemental line scan of the interface between the geopolymer (rich in Al and Si) and aluminum confirms that the crack is debonding between the layers. Elemental amounts are shown in weight %.

5.3 Analysis of Flux Rates

The comparison of permeate flux through the membranes in end-flow and cross-flow filtration show the decided difference between the two filtration modes. As discussed earlier, cross-flow filtration was expected to have much higher and steadier flux through the membrane due to less caking on the surface of the membrane.

In Figure 5.7, permeate flux is plotted against permeate volume for end-flow filtration results at 30 PSI and 40 PSI. Error bars are also shown. There was a large variation in data at the onset of filtration, which was a common occurrence for all the end-flow and cross-flow samples. It could be that at the onset of filtration, before caking on the membrane surface has begun, the variation in flux may be more representative of the variation in the porosity and thickness of the membranes themselves. Following Darcy's law correlating flux to the resistance due to caking, a power law trendline was used to model the data with the following R^2 values: 0.8359 (30 PSI), 0.8501 (40 PSI). Noteworthy is that the 30 PSI samples struggled to filter the complete 290 mL of produced water, resulting in limited data after approximately 220 mL; this is due to the low pressure being unable to overcome the resistance due to caking on the surface of the membrane.

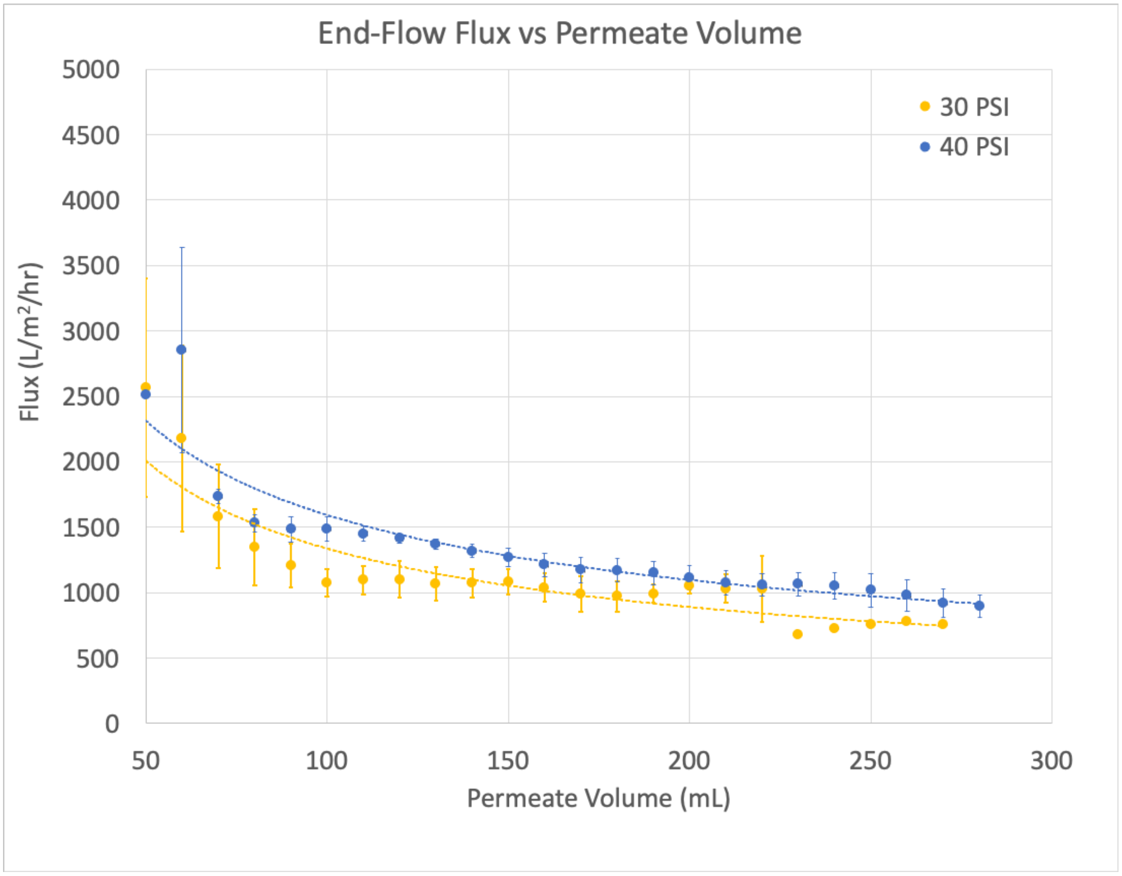

Figure 5.7 Plot of permeate flux vs permeate volume for end-flow filtration at 30 PSI and 40 PSI.

For end-flow filtration, Figure 5.8 shows a plot of permeate flux vs time. Similar to the previous plot, the results show the expected decrease in flux as resistance due to caking increases over time. A power trendline was used to model the data with the following R^2 values: 0.9080 (30 PSI), 0.9705 (40 PSI).

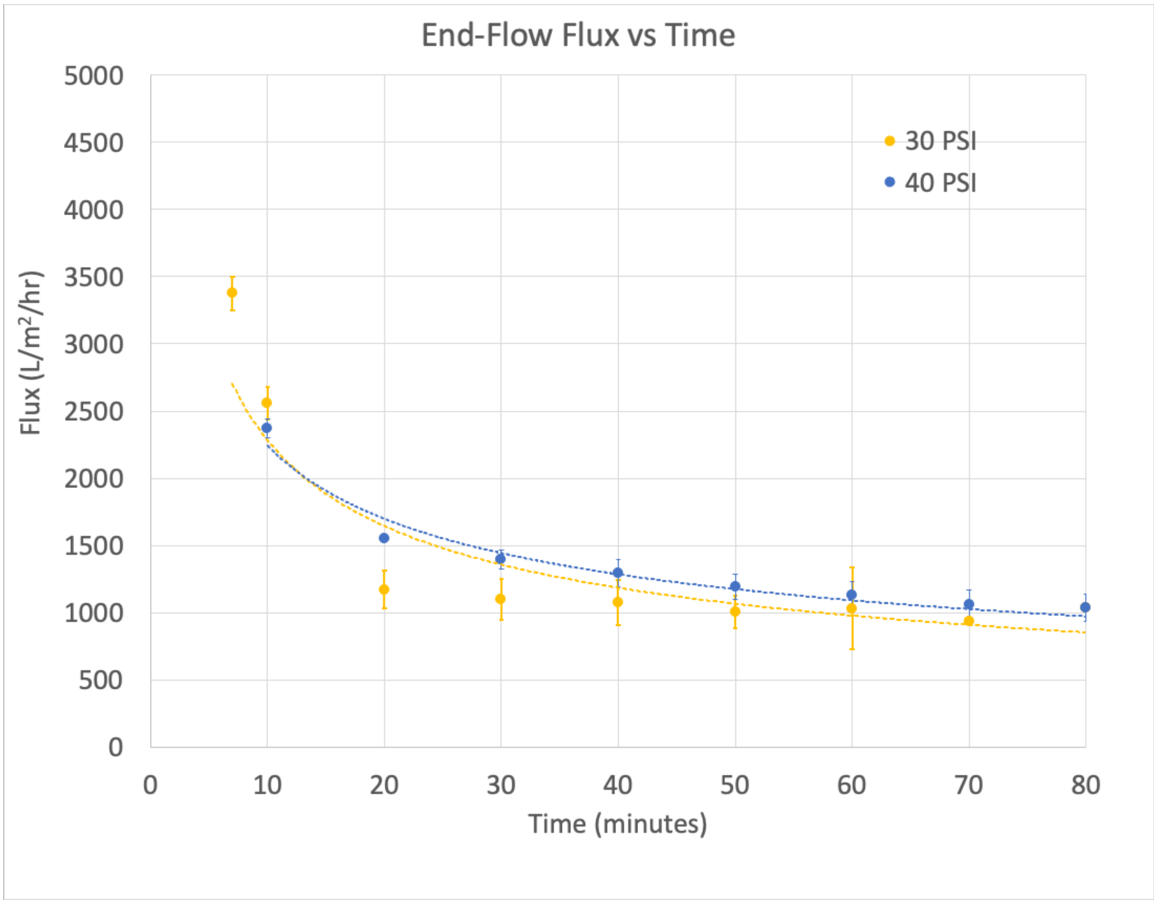

Figure 5.8 Permeate flux vs time for end-flow filtration of produced water at 30 PSI and 40 PSI.

For cross-flow filtration, plots are shown in Figure 5.9 and 5.10 for permeate flux vs permeate volume and permeate flux vs time, respectively. The variation in data is much more significant than with the end-flow results. This is likely due to nature of cross-flow filtration: the flux through the membrane is less dependent on the caking layer on the surface of the membrane and more dependent on the thickness and porosity of the membrane itself. As time goes on, the resistance due to caking will eventually increase and dominate the flux. Note that the 100 RPM results start at 100 mL; this is for consistency, as some cross-flow samples had such quick filtration that the first volume data point was obtained at 100 mL in less than 10 minutes (see Figure 5.10 with the large variation in initial data at approximately 7 minutes). At approximately 200 mL mark in Figure 5.6 and at 10 minutes in Figure 5.10, the 75 RPM results temporarily overtake the 100 RPM results; this is most likely due to the large variation in data with the cross-flow results as indicated by the overlapping error bars. A power trendline was applied to both plots with R^2 values for permeate flux vs permeate volume at 0.6979 (75 RPM) and 0.8736 (100 RPM), and for permeate flux vs time at 0.9503 (75 RPM) and 0.8839 (100 RPM).

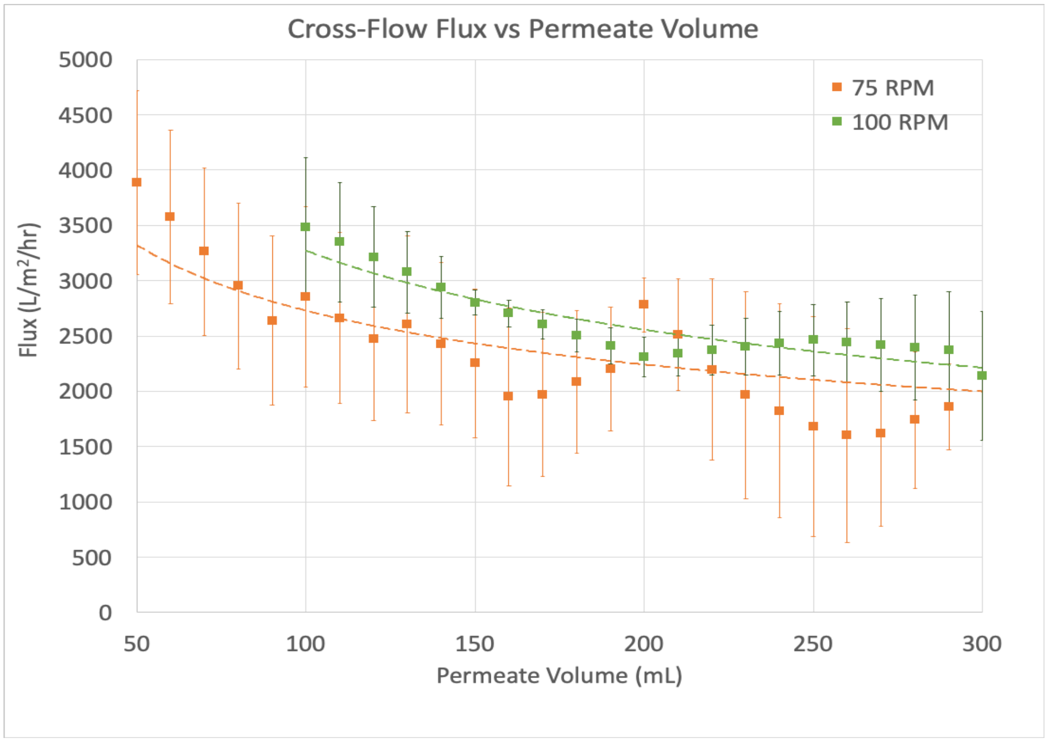

Figure 5.9 Permeate flux vs permeate volume for cross-flow filtration samples.

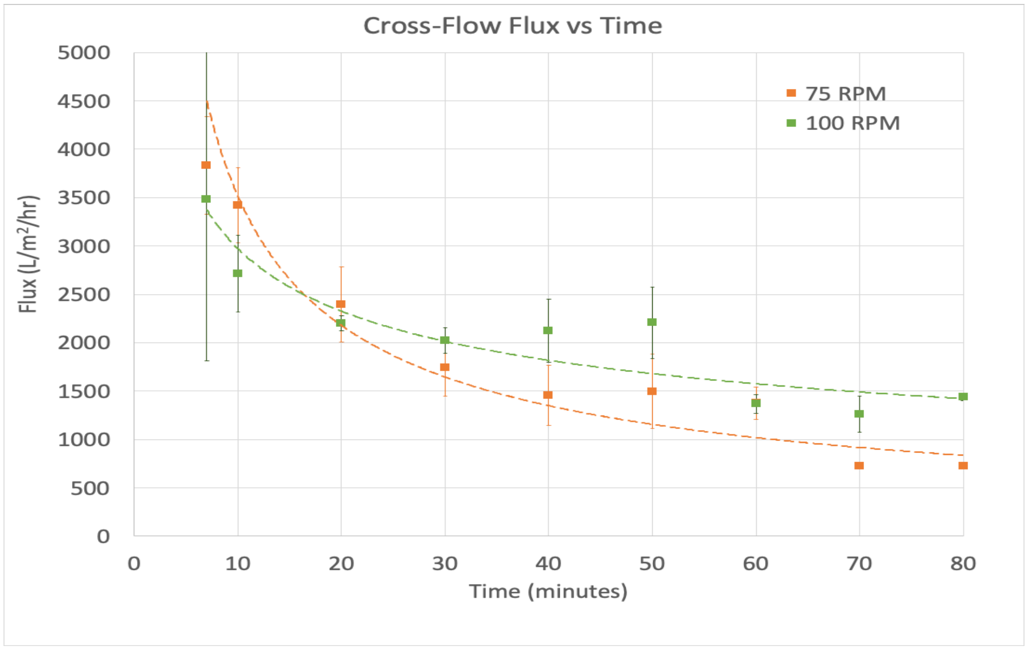

Figure 5.10 Permeate flux vs time for cross-flow filtration samples.

A comparison of both end-flow and cross-flow results is shown in Figure 5.11 and Figure 5.12. In Figure 5.11, the cross-flow results had much higher flux than the end-flow results, as was expected. There was also much more variation and less fit to the power regression for the cross-flow results, again likely due to the flux being more dependent on the variation in individual membrane properties rather than the resistance due to caking. When comparing the flux vs time for end-flow and cross-flow filtration modes in Figure 5.12, the impact of low flow speeds becomes apparent. For the 75 RPM samples, the flux drops off very quickly, meeting the flux of the end-flow results. Consistent with the turbidity results, this is most likely due to the flow rate of the feed and retentate streams being too low to carry away caking particles, and instead the samples are experiencing filtration more similar to end-flow with particles building up on the surface of the membranes.

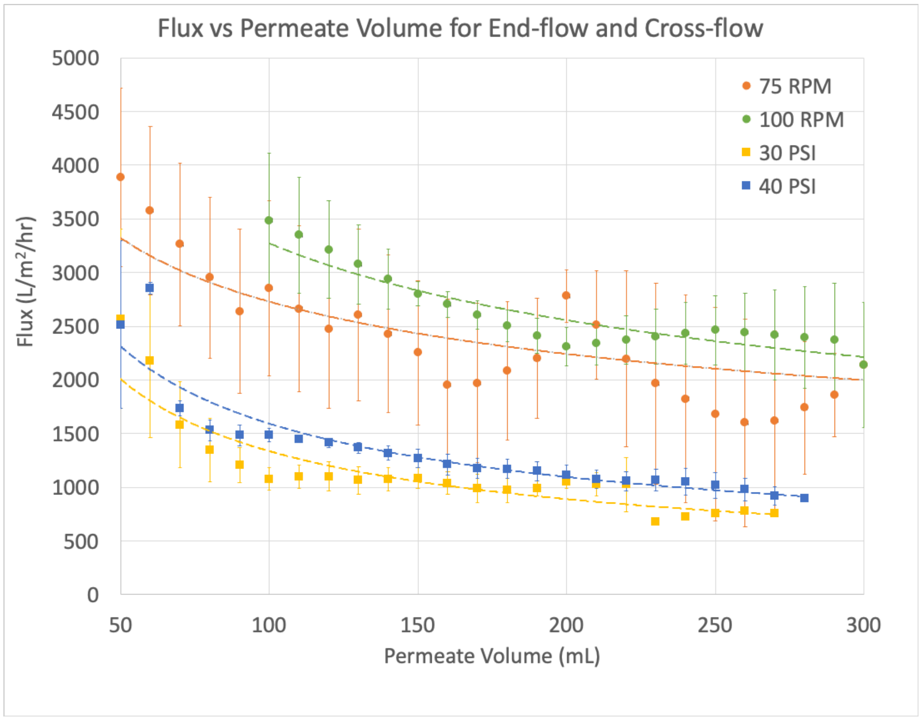

Figure 5.11 Permeate flux vs permeate volume for end-flow and cross-flow filtration of produced water using geopolymer composite membranes.

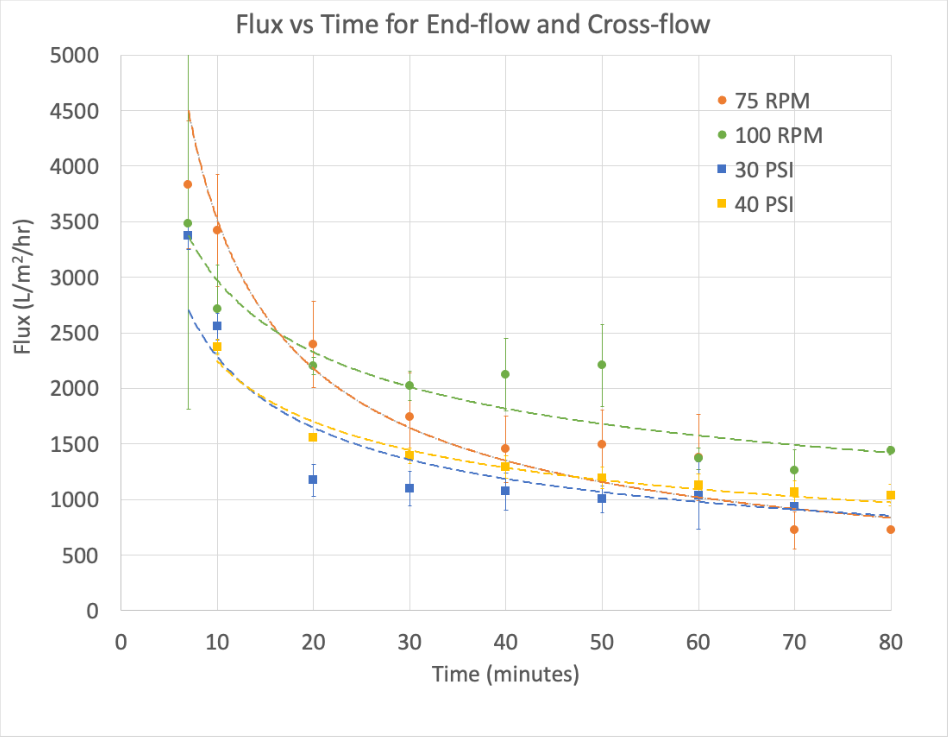

Figure 5.12 Permeate flux vs time for end-flow and cross-flow filtration results.

A plot of permeate volume vs time for end-flow and cross-flow filtration is shown in Figure 5.13. Once again, it is seen that the cross-flow samples had significantly higher permeate volumes when compared to end-flow. The data for the 75 RPM samples appears to show a decrease in volume, but this is due to variation in the data as well as the reduced filtration due to caking as time went on.

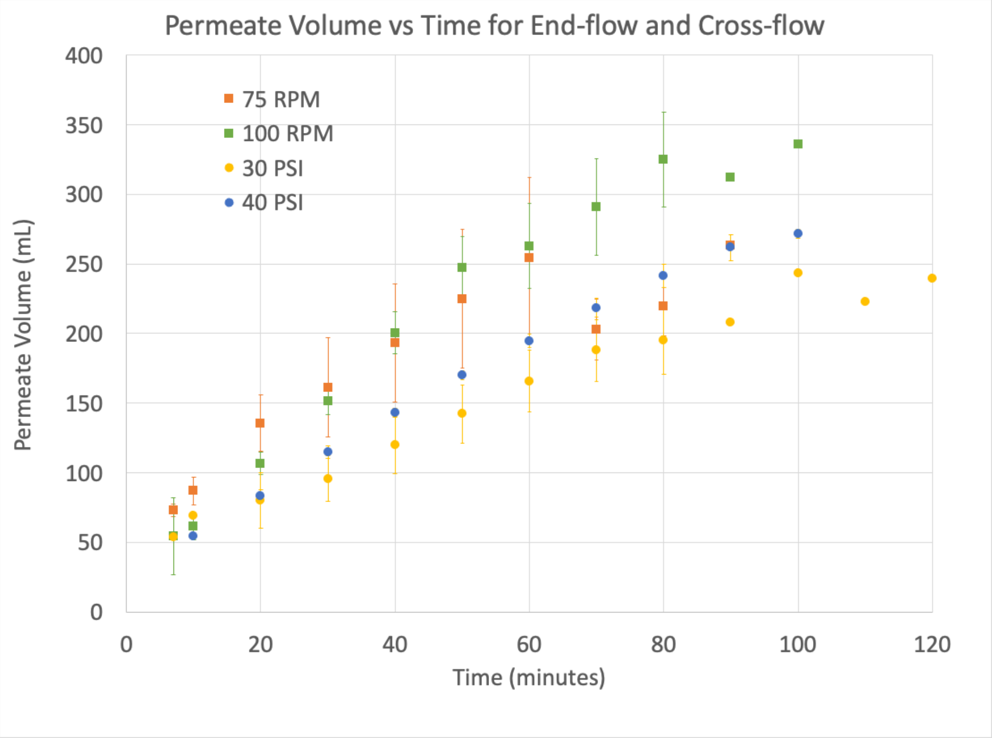

Figure 5.13 Permeate volume vs time for end-flow and cross-flow filtration results.

Overall, the 100 RPM cross-flow filtration results showed the most promise for filtration of produced water with the highest permeate flux over time through the geopolymer composite membranes and higher reduction in turbidity. As 100 RPM was the maximum pump speed available for these experiments, it is possible that at even higher pump speeds the flux could be increased and the turbidity reduced even further.

CHAPTER VI

CONCLUSIONS AND FUTURE WORK

This study explored the development of a low-cost self-supporting geopolymer composite membrane for filtration of produced water, and the comparison of the filtration performance of the membranes in end-flow and cross-flow filtration modes. Key findings as well as suggestions for future work are summarized in this chapter.

6.1 Conclusions

- The optimum composition for the geopolymer composite membranes was found to be $K_2O \cdot Al_2O_3 \cdot 2SiO_2 \cdot 11H_2O$ for structural stability, reduced microcracking, and feasible curing times. The optimum curing conditions were found to be 36 hours at 60 ºC and 40% humidity, followed by a controlled temperature reduction to 20 ºC over 5 hours.
- The addition of zeolite to the geopolymer reduced any visual microcracking when bonding with the aluminum substrate, although microcracking and debonding was visible in optical microscopy and SEM images.

- The minimum pore size of the samples was analyzed using MIP and found to be approximately 0.480 μm, and the porosity to be 24.3%.
- Cross-flow filtration has much higher permeate flux and reduction in turbidity than end-flow filtration but must be run at high water flow speeds to ensure the retentate carries out particles and prevent caking.
- Overall, the geopolymer composite membranes did filter the produced water, but more work needs to be done to improve filtration through better bonding of the interface between the ceramic layer and the aluminum layer, reduce microcracks, and potentially reduce conductivity and TDS values for filtered produced water..
- Compared to current produced water membrane treatment methods, the geopolymer composite membranes developed in this study are low in cost due to the use of inexpensive raw material and low processing temperatures. With the limited reduction in conductivity of treated water, these geopolymer composite membranes would need to be used in a multi-step treatment process for complete treatment of produced water. This is expected, as there is currently no single-step treatment method for produced water that removes all contaminants.

6.2 Future Work

Based on the conclusions of this study, promising directions for future work are described below:

- Development of thinner membranes, possibly using a hydraulic press or other means that would have a higher applied load than was used in this study.

- Improvement of bond between the geopolymer composite and aluminum: possibly varying the aluminum alloy.
- Improved filtration: even higher permeate flux may be obtainable with higher pump speeds. Reduction in TDS may be achieved with smaller pore sizes.
- Temperature studies: this study was conducted using room temperature produced water, but feedwater in industry may vary across a range of temperatures. It would be interesting and useful to conduct experiments across a varying range (both low and high temperatures) to see the impact on the membrane filtration.
- Tubular geometry: for scale-up and industry application, the geopolymer composite membrane would need to be adapted to a tubular geometry that would be portable and adaptable to existing piping structure in the field
- Performance of geopolymer composite membranes after backwashing should be characterized.

REFERENCES

[1] Clack, C.E., Veil, J.A (Environmental Science Division, Argonne National Laboratory). *Produced Water Volumes and Management Practices in the United States*. 2009.

[2] Veil, John A. "Produced Water Management Options and Technologies." *Produced Water*, 2011, doi:10.1007/978-1-4614-0046-2_29.

[3] Heggie, Jon. "Why Is America Running Out of Water?" *NationalGeographic.com*, National Geographic, 12 August 2020, https://www.nationalgeographic.com/science/article/partner-content-americas-looming-water-crisis

[4] Al-Ghouti, Mohammad A., et al. "Produced Water Characteristics, Treatment and Reuse: A Review." *Journal of Water Process Engineering*, vol. 28, no. February, Elsevier, 2019, pp. 222–39, doi:10.1016/j.jwpe.2019.02.001.

[5] Nasiri, Masoud, et al. "Oil and Gas Produced Water Management: A Review of Treatment Technologies, Challenges, and Opportunities." *Chemical Engineering Communications*, vol. 204, no. 8, 2017, pp. 990–1005, doi:10.1080/00986445.2017.1330747.

[6] Pearce, Graeme K. "Membrane Filtration for Wastewater Reuse: Current Status and Future Developments." *Water and Wastewater International*, vol. 25, no. 5, 2010.

[7] Seader, J D, and Ernest J. Henley. Separation Process Principles. Chichester: John Wiley, 2005.

[8] Bhave, Ramesh R. “A Cross Flow Filtration Apparatus.” *Filtration + Separation*, vol. 37, no. 6, 2000, p. 29, doi:10.1016/s0015-1882(00)89238-1.

[9] Cui, Z. F., and H. S. Muralidhara. “Fundamentals of pressure-driven membrane separation processes.” *Membrane Technology : a Practical Guide to Membrane Technology and Applications in Food and Bioprocessing* . 1st ed. Amsterdam ;: Butterworth-Heinemann, 2010.

[10] Schwartz, Larry, and Kevin Seeley. Introduction to Tangential Flow Filtration for Laboratory and Process Development Applications. 2014.

[11] Balster, Joerg. “Encyclopedia of Membranes.” *Encyclopedia of Membranes*, 2013, pp. 3–5, doi:10.1007/978-3-642-40872-4.

[12] Abdullayev, Amanmyrat, et al. “Materials and Applications for Low-Cost Ceramic Membranes.” *Membranes*, vol. 9, no. 9, 2019, doi:10.3390/membranes9090105.

[13] Davidovits, J. Geopolymers and geopolymeric materials. *Journal of Thermal Analysis and Calorimetry*. 1989; v35, no. 2, p. 429-441.

[14] Della Rocca, Daniela Gier, et al. “Adding Value to Aluminosilicate Solid Wastes to Produce Adsorbents, Catalysts and Filtration Membranes for Water and Wastewater Treatment.” *Journal of Materials Science*, vol. 56, no. 2, 2021, pp. 1039–63, doi:10.1007/s10853-020-05276-0.

[15] Zhang, Peng, et al. “Fabrication and Engineering Properties of Concretes Based on Geopolymers/Alkali-Activated Binders - A Review.” *Journal of Cleaner Production*, vol. 258, Elsevier Ltd, 2020, p. 120896, doi:10.1016/j.jclepro.2020.120896.

[16] Duxson, P., et al. “Geopolymer Technology: The Current State of the Art.” *Journal of Materials Science*, vol. 42, no. 9, 2007, pp. 2917–33, doi:10.1007/s10853-006-0637-z.

[17] Azarsa, Peiman, and Rishi Gupta. “Durability and Leach-Ability Evaluation of K-Based Geopolymer Concrete in Real Environmental Conditions.” *Case Studies in Construction Materials*, vol. 13, Elsevier Ltd., 2020, p. e00366, doi:10.1016/j.cscm.2020.e00366.

[18] Bell, Jonathan, et al. Use of Geopolymeric Cements as a Refractory Adhesive for Metal and Ceramic Joins. 2008, pp. 407–13, doi:10.1002/9780470291238.ch46.

[19] Rego, S. R., et al. “Application of Geopolymeric Adhesives in Ceramic Systems Subjected to Cyclic Temperature Environments.” *Journal of Adhesion*, vol. 90, no. 1, 2014, pp. 120–33, doi:10.1080/00218464.2013.794109.

[20] De Barros, S., et al. “Adhesion of Geopolymer Bonded Joints Considering Surface Treatments.” *Journal of Adhesion*, vol. 88, no. 4–6, 2012, pp. 364–75, doi:10.1080/00218464.2012.660075.

[21] Rong, Xian, et al. “Review on the Adhesion of Geopolymer Coatings.” *ACS Omega*, vol. 6, no. 8, 2021, pp. 5108–12, doi:10.1021/acsomega.0c06343.

[22] Temuujin, Jadambaa, et al. “Preparation of Metakaolin Based Geopolymer Coatings on Metal Substrates as Thermal Barriers.” *Applied Clay Science*, vol. 46, no. 3, Elsevier B.V., 2009, pp. 265–70, doi:10.1016/j.clay.2009.08.015.

[23] Mao, Yangwu, et al. “Metakaolin-Based Geopolymer Coatings on Metals by Airbrush Spray Deposition.” *Journal of Coatings Technology and Research*, vol. 17, no. 4, Springer US, 2020, pp. 991–1002, doi:10.1007/s11998-019-00310-6.

[24] Ge, Yuanyuan, et al. “Preparation of Geopolymer-Based Inorganic Membrane for Removing Ni2+ from Wastewater.” *Journal of Hazardous Materials*, vol. 299, Elsevier B.V., 2015, pp. 711–18, doi:10.1016/j.jhazmat.2015.08.006.

[25] Novais, Rui M., et al. “Novel Porous Fly-Ash Containing Geopolymer Monoliths for Lead Adsorption from Wastewaters.” *Journal of Hazardous Materials*, vol. 318, Elsevier B.V., 2016, pp. 631–40, doi:10.1016/j.jhazmat.2016.07.059.

[26] Onutai, Sujitra, et al. “Porous Fly Ash-Based Geopolymer Composite Fiber as an Adsorbent for Removal of Heavy Metal Ions from Wastewater.” *Materials Letters*, vol. 236, Elsevier B.V., 2019, pp. 30–33, doi:10.1016/j.matlet.2018.10.035.

[27] Hu, Sixian, et al. “Synthesis of Rare Earth Tailing-Based Geopolymer for Efficiently Immobilizing Heavy Metals.” *Construction and Building Materials*, vol. 254, Elsevier Ltd, 2020, p. 119273, doi:10.1016/j.conbuildmat.2020.119273.

[28] Zhang, Jin, et al. “Synthesis of a Self-Supporting Faujasite Zeolite Membrane Using Geopolymer Gel for Separation of Alcohol/Water Mixture.” *Materials Letters*, vol. 116, 2014, pp. 167–70, doi:10.1016/j.matlet.2013.11.008.

[29] Xu, Meng xue, et al. “Preparation and Characterization of a Self-Supporting Inorganic Membrane Based on Metakaolin-Based Geopolymers.” *Applied Clay Science*, vol. 115, Elsevier B.V., 2015, pp. 254–59, doi:10.1016/j.clay.2015.03.019.

[30] Xu, Meng-xue, et al. “Preparation of Geopolymer Inorganic Membrane and Purification of Pulp-Papermaking Green Liquor.” *Applied Clay Science*, vol. 168, Elsevier Ltd, Feb. 2019, pp. 269–75, doi:10.1016/j.clay.2018.11.024.

[31] Hajimohammadi, Ailar, et al. “Regulating the Chemical Foaming Reaction to Control the Porosity of Geopolymer Foams.” *Materials and Design*, vol. 120, Elsevier Ltd, 2017, pp. 255–65, doi:10.1016/j.matdes.2017.02.026.

[32] Bai, Chengying, and Paolo Colombo. “Processing, Properties and Applications of Highly Porous Geopolymers: A Review.” *Ceramics International*, vol. 44, no. 14, Elsevier Ltd, 1 Oct. 2018, pp. 16103–18, doi:10.1016/j.ceramint.2018.05.219.

[33] Ducman, V., and L. Korat. “Characterization of Geopolymer Fly-Ash Based Foams Obtained with the Addition of Al Powder or H2O2 as Foaming Agents.” *Materials Characterization*, vol. 113, Elsevier B.V., 2016, pp. 207–13, doi:10.1016/j.matchar.2016.01.019.

[34] Novais, Rui M., et al. “Geopolymer Foams: An Overview of Recent Advancements.” *Progress in Materials Science*, vol. 109, no. July 2019, 2020, doi:10.1016/j.pmatsci.2019.100621.

[35] Bai, Chengying, and Paolo Colombo. “High-Porosity Geopolymer Membrane Supports by Peroxide Route with the Addition of Egg White as Surfactant.” *Ceramics International*, vol. 43, no. 2, Elsevier, 2017, pp. 2267–73, doi:10.1016/j.ceramint.2016.10.205.

[36] Hajimohammadi, Ailar, et al. “Pore Characteristics in One-Part Mix Geopolymers Foamed by H 2 O 2 : The Impact of Mix Design.” *Materials and Design*, vol. 130, no. May, Elsevier, 2017, pp. 381–91, doi:10.1016/j.matdes.2017.05.084.

[37] Yan, Shu, et al. “Green Synthesis of High Porosity Waste Gangue Microsphere/Geopolymer Composite Foams via Hydrogen Peroxide Modification.” *Journal of Cleaner Production*, vol. 227, Elsevier Ltd, 2019, pp. 483–94, doi:10.1016/j.jclepro.2019.04.185.

[38] Cilla, Marcelo S., et al. “Geopolymer Foams Obtained by the Saponification/Peroxide/Gelcasting Combined Route Using Different Soap Foam Precursors.” *Journal of the American Ceramic Society*, vol. 100, no. 8, 2017, pp. 3440–50, doi:10.1111/jace.14902.

[39] Bai, Chengying, et al. “High-Porosity Geopolymer Foams with Tailored Porosity for Thermal Insulation and Wastewater Treatment.” *Journal of Materials Research*, vol. 32, no. 17, Cambridge University Press, Sept. 2017, pp. 3251–59, doi:10.1557/jmr.2017.127.

[40] Bai, Chengying, et al. “High Strength Metakaolin-Based Geopolymer Foams with Variable Macroporous Structure.” *Journal of the European Ceramic Society*, vol. 36, no. 16, Elsevier Ltd, 2016, pp. 4243–49, doi:10.1016/j.jeurceramsoc.2016.06.045.

[41] Petlitckaia, Svetlana, and Arnaud Poulesquen. “Design of Lightweight Metakaolin Based Geopolymer Foamed with Hydrogen Peroxide.” *Ceramics International*, vol. 45, no. 1,

Elsevier Ltd and Techna Group S.r.l., 2019, pp. 1322–30, doi:10.1016/j.ceramint.2018.10.021.

[42] Xu, Ying. Studies on the Use of Metakaolin Geopolymer for Produced Water Treatment. 2019. Oklahoma State University, M.S. dissertation.

[43] Natali Murri, Annalisa, et al. “Porous Geopolymer Insulating Core from a Metakaolin/Biomass Ash Composite.” *Environments*, vol. 4, no. 4, 2017, p. 86, doi:10.3390/environments4040086.

[44] Novais, Rui M., et al. “Porous Biomass Fly Ash-Based Geopolymers with Tailored Thermal Conductivity.” *Journal of Cleaner Production*, vol. 119, 2016, pp. 99–107, doi:10.1016/j.jclepro.2016.01.083.

[45] Liu, Yi, et al. “One-Step Fabrication of Novel Porous and Permeable Self-Supporting Zeolite Block from Fly Ash.” *Materials Letters*, vol. 196, Elsevier B.V., 2017, pp. 328–31, doi:10.1016/j.matlet.2017.03.097.

[46] Zhang, Zuhua, et al. “Novel Self-Supporting Zeolitic Block with Tunable Porosity and Crystallinity for Water Treatment.” *Materials Letters*, vol. 178, Elsevier, 2016, pp. 151–54, doi:10.1016/j.matlet.2016.04.214.

[47] Naveed, Amir, et al. “Synthesis and Characterization of Fly Ash Based Geopolymeric Membrane for Produced Water Treatment.” *Desalination and Water Treatment*, vol. 161, no. July, 2019, pp. 126–31, doi:10.5004/dwt.2019.24283.

[48] Kuenzel, C., et al. “Encapsulation of Aluminum in Geopolymers Produced from Metakaolin.” *Journal of Nuclear Materials*, vol. 447, no. 1–3, Elsevier B.V., 2014, pp. 208–14, doi:10.1016/j.jnucmat.2014.01.015.

[49] Kennedy, D. A., et al. “Cation Exchange Modification of Clinoptilolite –Thermodynamic Effects on Adsorption Separations of Carbon Dioxide, Methane, and Nitrogen.” *Microporous*

and Mesoporous Materials, vol. 274, no. November, 2019, pp. 327–41, doi:10.1016/j.micromeso.2018.08.035.

[50] Rusydi, Anna F. “Correlation between Conductivity and Total Dissolved Solid in Various Type of Water: A Review.” *IOP Conference Series: Earth and Environmental Science*, vol. 118, no. 1, 2018, doi:10.1088/1755-1315/118/1/012019.

[51] Guerra, Katie, et al. “Oil and Gas Produced Water Management and Beneficial Use in the Western United States.” *U.S. Department of the Interior Bureau of Reclamation, Managing Water in the West*, no. 157, 2011, p. 129, http://www.usbr.gov/research/AWT/reportpdfs/report157.pdf.

APPENDICES

APPENDIX A

Determination of Conductivity Factor using TDS Experiments

Table 7.1 Experimental data from TDS experiments to determine conductivity factor. All samples of produced water were taken from the same barrel obtained from the Anadarko Shelf in Oklahoma.

Sample #	Initial Beaker Weight (g)	Measured Conductivity (µS/cm)	Final Weight with TDS (g)	TDS Residue (mg/L)	Calculated Conductivity Factor (k_e)
Produced Water #1	115.6434	157,860	135.7934	201.500	1.27645
			135.7425	200.991	1.27322
Produced Water #2	118.3625	157,860	138.8970	205.345	1.3008
			138.8437	204.812	1.29743
Produced Water #3	117.5781	157,860	138.0165	204.384	1.29472
			137.9723	203.942	1.29192

APPENDIX B

End-flow Filtration Water Quality and Flux Results

Table 7.2 Sample water quality results for end-flow filtration.

Sample #	Thickness (mm)	Pressure (PSI)	Turb. Before (NTU)	Turb. After (NTU)	pH Before	pH After	Cond. Before (µS/cm)	Cond. After (µS/cm)
E1	2.034	30	52.3	13.6	6.812	7.822	238,840	156,700
E2	1.938	30	68.3	14.9	7.152	7.344	135,100	137,200
E3	2.755	30	58.6	12.3	6.819	7.323	90,000	78,000
E4	2.393	40	80.4	8.17	6.616	7.860	238,670	198,700
E5	2.147	40	80.4	26.8	6.616	7.329	238,670	218,170
E6	2.243	40	68.3	12.5	7.152	7.475	135,100	129,400

Table 7.3 Sample permeate flux results for end-flow filtration.

E1	30 PSI		E2	30 PSI	
Perm. Vol. (mL)	Time (min)	Flux (L/m^2/hr)	Perm. Vol. (mL)	Time (min)	Flux (L/m^2/hr)
65	25	1158.5	50	6.2	3593.4
100	37	1299.6	75	11.2	2227.9
130	48	1215.2	90	15.6	1507.6
150	55	1273.1	100	19.9	1044.3
170	62	1273.1	120	26.9	1279.2
190	70	1113.9	135	32.6	1172.6
220	80	1336.7	150	38.7	1092.7
225	90	222.79	165	45.8	937.0
275	97	222.79	195	58.8	1029.6
280	101	3182.7	215	67.9	979.3
290	105	557.0	220	71.4	639.6
E3	30 PSI		E4	40 PSI	
Perm. Vol. (mL)	Time (min)	Flux (L/m^2/hr)	Perm. Vol. (mL)	Time (min)	Flux (L/m^2/hr)
50	14.4	1543.6	60	13.6	1968.2
80	30.5	831.1	75	18.1	1479.8
105	43.0	893.5	120	33.0	1345.7
125	55.0	743.7	150	44.3	1188.2
155	69.6	912.4	170	52.9	1034.2
175	82.7	682.9	210	71.8	943.0
200	94.4	949.4	225	78.8	950.3
225	111.3	657.8	262	96.1	953.0
245	123.2	751.0	275	103.8	749.0
260	131.8	775.7	285	109.0	868.0
275	140.8	741.3			

E5	40 PSI		E6	40 PSI	
Perm. Vol. (mL)	Time (min)	Flux ($L/m^2/hr$)	Perm. Vol. (mL)	Time (min)	Flux ($L/m^2/hr$)
65	15.6	1854.6	50	8.87	2512.7
85	22.5	1304.1	75	15.5	1679.3
130	36.3	1449.5	100	22.1	1700.7
175	50.7	1389.2	130	31.9	1361.7
220	66.7	1257.1	165	56.5	1069.4
250	77.0	1293.6	185	54.2	1147.4
290	94.3	1030.2	215	68.0	969.9
			235	77.2	970.4
			255	89.1	748.9
			290	108.7	796.4

Table 7.4 Trendline and R^2 values for end-flow results.

	Graph	Power Trendline	R^2 Value
30 PSI	Perm. Flux vs Perm. Vol.	$y = 19982x^{-0.587}$	0.8359
40 PSI	Perm. Flux vs Perm. Vol.	$y = 19025x^{-0.539}$	0.8501
30 PSI	Perm. Flux vs Time	$y = 6787.2x^{-0.473}$	0.9080
40 PSI	Perm. Flux vs Time	$y = 5663.6x^{-0.402}$	0.9705

APPENDIX C

Cross-flow Filtration Water Quality and Flux Results

Table 7.5 Sample water quality results for cross-flow filtration.

Sample #	Thickness (mm)	Pump Speed	Turb. Before (NTU)	Turb. After (NTU)	pH Before	pH After	Cond. Before (µS/cm)	Cond. After (µS/cm)
C1	2.280	75	57.9	6.81	6.772	7.157	89,300	76,500
C2	2.277	75	71.1	15.7	6.167	6.993	104,850	71,500
C3	1.922	75	67.1	5.00	7.016	7.433	91,100	80,300
C4	2.268	100	54.6	20.4	6.910	7.473	164,933	172,200
C5	2.522	100	55.4	22.5	6.815	7.086	105,100	95,100
C6	1.830	100	61.7	0.2	6.981	7.344	92,800	76,700

Table 7.6 Sample flux results for cross-flow filtration.

C1	75 RPM		C2	75 RPM	
Perm. Vol. (mL)	Time (min)	Flux (L/m^2/hr)	Perm. Vol. (mL)	Time (min)	Flux (L/m^2/hr)
50	4.0	5593.0	50	9.0	2489.3
100	8.7	4723.4	100	26.8	1247.0
150	15.2	3427.5	150	48.2	1044.3
200	22.1	3244.5	160	63.1	299.0
250	30.4	2673.5	192	81.2	785.6
300	40.8	2142.2			
350	50.8	2235.3			
400	62.0	1977.4			
C3	75 RPM		C4	100 RPM	
Perm. Vol. (mL)	Time (min)	Flux (L/m^2/hr)	Perm. Vol. (mL)	Time (min)	Flux (L/m^2/hr)
50	4.4	5025.3	50	6.22	3583.7
100	18.6	1572.6	100	15.38	2430.4
150	38.2	1137.6	150	25.62	2177.1
165	47.7	703.5	200	37.4	1898.8
200	54.2	2405.4	250	46.6	2421.6
225	64.2	1115.8	300	54.1	2963.9
250	80.4	686.9			
265	91.4	604.9			
300	100	1816.9			
C5	100 RPM		C6	100 RPM	
Perm. Vol. (mL)	Time (min)	Flux (L/m^2/hr)	Perm. Vol. (mL)	Time (min)	Flux (L/m^2/hr)

100	6.15	7245.2	50	9.6	2328.8
150	10.5	5141.3	100	20.5	2037.7
200	17.4	3244.5	150	33.9	1662.6
250	23.8	3454.1	200	48.8	1496.9
300	30.5	3350.2	250	70.8	1012.8
350	38.2	2893.4	300	84.8	1591.4
400	45.8	2918.6	350	106.0	1051.7

Table 7.7 Trendline and R^2 values for cross-flow results.

	Graph	Power Trendline	R^2 Value
75 RPM	Perm. Flux vs Perm. Vol.	$y = 10081x^{-0.284}$	0.6979
100 RPM	Perm. Flux vs Perm. Vol.	$y = 16885x^{-0.356}$	0.8736
75 RPM	Perm. Flux vs Time	$y = 17260x^{-0.691}$	0.9503
100 RPM	Perm. Flux vs Time	$y = 6729.9x^{-0.355}$	0.8839

VITA

Christine Ann Watson

Candidate for the Degree of

Master of Science

Thesis: LOW-COST CERAMIC COMPOSITE MEMBRANES FOR FILTRATION OF PRODUCED WATER

Major Field: Materials Science and Engineering

Biographical:

Education:

Completed the requirements for the Master of Science Materials Science and Engineering at Oklahoma State University, Stillwater, Oklahoma in December, 2021.

Completed the requirements for the Bachelor of Science in Chemical Engineering at North Carolina State University, Raleigh, North Carolina in 2009.

Completed the requirements for the Bachelor of Science in Physics at North Carolina State University, Raleigh, North Carolina in 2009.

Experience:

Graduate Teaching Assistant, Oklahoma State University, Stillwater/Tulsa, Oklahoma (2020-2021)

Graduate Research Assistant, Oklahoma State University, Tulsa, Oklahoma (2019-2021)

Intern, Department of Energy, Minority Educational Institution Student Partnership Program, Washington D.C. (2020)